Ann. Geophysicae 11, 395–418 (1993)

Annales Geophysicae

The atmospheric momentum budget over a major mountain range: first results of the PYREX field program

P. Bougeault [1], A. Jansa [2], J. L. Attie [3], I. Beau [1], B. Benech [3], R. Benoit [7], P. Bessemoulin [1], J. L. Caccia [12], J. Campins [2], B. Carissimo [4], J. L. Champeaux [1], M. Crochet [12], A. Druilhet [3], P. Durand [3], A. Elkhalfi [4], P. Flamant [13], A. Genoves [2], M. Georgelin [3], K. P. Hoinka [8], V. Klaus [1], E. Koffi [3], V. Kotroni [9], C. Mazaudier [9], J. Pelon [5], M. Petitdidier [9], Y. Pointin [6], D. Puech [1], E. Richard [3], T. Satomura [10], J. Stein [1], and D. Tannhauser [11]

[1] Météo-France, Centre National de Recherches Météorologiques, F-31057 Toulouse, France
[2] Instituto Nacional de Meteorologia, E-07015 Palma de Mallorca, Spain
[3] Laboratoire d'Aérologie, Université Paul Sabatier, F-31062 Toulouse, France
[4] Electricité de France, Direction des Etudes et Recherches, F-78401 Chatou, France
[5] Service d'Aéronomie du CNRS, Université Paris VI, F-75252 Paris, France
[6] Laboratoire de Météorologie Physique, Université Blaise Pascal, F-63000 Clermont-Ferrand, France
[7] Environnement Canada, Recherches en Prévision Numérique, Dorval H9P 1J3, Canada
[8] Deutsche Forschungsanstalt für Luft und Raumfahrt, W-8031 Oberpfaffenhofen, Germany
[9] Centre de Recherches en Physique de l'Environment, F-94107 Saint-Maur, France
[10] Meteorological Research Institute, Tsukuba, Ibaraki 305, Japan
[11] Department of Physics, Technion, 32000 Haifa, Israel
[12] Laboratoire de Sondages Electromagnétiques de l'Environnement Terrestre, Université de Toulon F-83957 La Garde, France
[13] Laboratoire de Météorologie Dynamique du CNRS F-91128 Palaiseau, France

Received October 9, 1992; revised January 18, 1993; accepted January 22, 1993

Abstract. The PYREX program is a major field study of the dynamical influence of the Pyrénées mountains (on the border between France and Spain) on the atmospheric circulation. In October and November 1990 a large number of experimental means had been deployed in the area, including additional sounding systems, automated stations at high elevation sites, wind profilers, sodars, constant level balloons, and four research airplanes. The main focus was on the quantification of the retardation of the cross-mountain flow by the range, but a number of related meso-scale phenomena had been captured, e.g. the formation of lee waves, lee eddies, sheltering areas, and local surface winds. The data interpretation was supported by an extensive effort in meso-scale numerical modelling, and it is argued that only numerical models, conveniently qualified by observations, can document the momentum budget in a consistent way. Improvements in the field of mountain waves and mountain roughness representation in the large-scale atmospheric models are expected from the PYREX results, as well as improvements in the performance of meso-scale models for the operational forecasts. The present paper presents a broad introduction to the experiment. It reviews the experimental set-up and the available data sets. Finally, two more specific topics are discussed in depth, as examples of the available data and modelling strategy: the lee wave event of 15 October 1990 is presented with both experimental and model results. Some of the findings concerning the Tramontana wind are also discussed.

Correspondence to: P. Bougeault

1 Introduction

Twenty years have passed since Lilly (1972) identified the orographic drag as a major sink of atmospheric momentum, leading to continued development of research on mountain influence on the atmosphere. During these two decades, his idea has been largely confirmed by experimental, numerical and theoretical work. Determinations of the surface pressure drag by major or modest mountain ranges are now available (e.g. Smith, 1978; Davies, 1987; Carissimo *et al.*, 1988), as well as altitude measurements of the wave momentum flux (Lilly *et al.*, 1982; Hoinka, 1987; Shutts, 1992). The ALPEX program (WMO, 1986) has provided a large number of high quality measurements around the Alps, and confirmed the existence of stagnation points in the atmosphere. Numerical models have transformed our approach to orographic processes, and led to the discovery of major nonlinear effects (e.g. Peltier and Clark, 1979; Durran and Klemp, 1987; Smolarkiewicz and Rotunno, 1989), having dramatic consequences on the actual weather patterns in mountain areas, like downslope windstorms, lee-side eddies, or upstream blocking. The theoretical understanding has also largely progressed (see the review by Smith, 1989). Meanwhile, some simple parameterization of the dynamical effects of meso-scale mountains in large-scale numerical models of the atmosphere have brought the largest improvements ever obtained in the forecast scores of these models (Boer *et al.*, 1984; Palmer *et al.*, 1986; Wallace *et al.*, 1983). The study of orographic effects has emerged as one of rich and still largely unexplored phenomenology, exciting theoretical problems, ideal test-bed for new instrumentation, and the key to drastic improvements of numerical forecasts, both at meso and larger scales, in-

Table 1. List of acronyms

Acronym	Full name	Affiliation
CNES	Centre national d'études spatiales	Ministry of Research (France)
CNRM	Centre National de Recherches Météorologiques	Météo-France and CNRS
CNRS	Centre National de la Recherche Scientifique	Ministry of Research (France)
CRPE	Centre de Recherche en Physique de l'Environnement	CNRS and CNET
DLR	Deutsche Forschungsanstalt für Luft- und Raumfahrt	Ministry of Research (Germany)
EDF	Electricité de France	Independent agency
ENM	Ecole Nationale de la Météorologie	Météo-France
IGN	Institut Géographique National	Independent agency
INM	Instituto Nacional de Meteorologia (Spanish Weather Service)	Ministry of Transport (Spain)
INSU	Institut National des Sciences de l'Univers	CNRS
LA	Laboratoire d'Aérologie	CNRS and Toulouse University
LAMP	Laboratoire de Météorologie Physique	CNRS and Clermont-Ferrand University
LMD	Laboratoire de Météorologie Dynamique	CNRS
LSEET	Laboratoire de Sondages Electromagnétiques de l'Environnement Terrestre	CNRS and University Toulon
Météo-France	French Weather Service	Ministry of Transport (France)
SA	Service d'Aéronomie	CNRS and Paris 6 University
UIB	Department of Physics	University of Balearic Islands
UV	Department of Physics	University of Valladolid

cluding climate models. It is therefore no surprise if the Météo-France proposal to conduct a major field study of the dynamical influence of the Pyrénées mountains on the atmospheric flow has received strong support from many agencies and institutes, and attracted several scientists from nearby countries. A list of these agencies is given in the acknowledgments section and a list of acronyms may be found in Table 1. The resulting field program, called PYREX, was described by Bougeault *et al.* (1990), and was conducted in October and November 1990. The aim of the present paper is to give a broad description of the experimental results, encountered phenomenology, available data-sets, and preliminary scientific conclusions.

The motivations of the different participants were explained in detail by Bougeault *et al.* (1990). In summary, they range from a better knowledge of the phenomenology of mean and turbulent wind and pressure patterns in the vicinity of the Pyrenean range, to an accurate, possibly operational, numerical modelling of these patterns, through an improved representation of the underlying dynamical processes, in connection with the most recent theories of orographic flows. A variety of meteorological phenomena are created by the Pyrénées: foehn effects on either side of the range, downslope windstorms, regional winds further in the plain, blocking etc. In order to understand these dynamics, it is necessary to develop a quantitative appraisal of the momentum budget. This will also help us understand how the retardation effect of the mountains affects the atmosphere at larger scales. There was, therefore, a high convergence of scientific interests, justifying a cooperative experimental program. However, the difficulty of deriving a reliable momentum budget from measurements only is well known, and it was felt more adequate to use numerical models to achieve this result. This resulted, from the beginning of the planning phase, in a high level of cooperation between the modelling and experimental approaches. The measurements were organized not only to document some of the most important terms of the momentum budget, such as the pressure drag and wave momentum fluxes, but also to validate other aspects of meso-beta scale numerical simulations. These numerical results will be used, under the control of existing observations, to derive the missing terms of the momentum budget over the instrumented areas, and all the terms of this budget over adjacent areas, or during periods when no special observations exist. This use of models as numerical laboratories has been illustrated in the past by the so-called large-eddy-simulation approach. Recently, it has been applied by Hoinka and Clark (1991), and Clark and Miller (1991) to flows over the Alps. These last studies are very close in essence to the foreseen scientific use of the PYREX data, but we think we can improve on their results, since we were fortunate enough to observe a wide variety of situations, with a large number of quality measurement systems.

Section 2 will briefly describe the experimental set-up, the encountered situations and the main existing data sets. This will be followed by a more precise discussion of two topics among the several possible (Sects. 3 and 4). Experimental results will be presented and compared with preliminary numerical results. We will try to derive some preliminary conclusions concerning the strategy in Sect. 5.

2 Overview of the experiment

To reach the above-mentioned objectives, it was necessary to use both an infrastructure of ground-based measurements, operating either continuously or on alert, and a fleet of research aircraft and constant-level balloons flying in coordination. A synoptic view of the ground infrastructure is given in Fig. 1, with a list of institutes responsible for operating facilities during PYREX in Table 2. We used the concept of Intensive Observation Period (IOP in the following), corresponding to the acti-

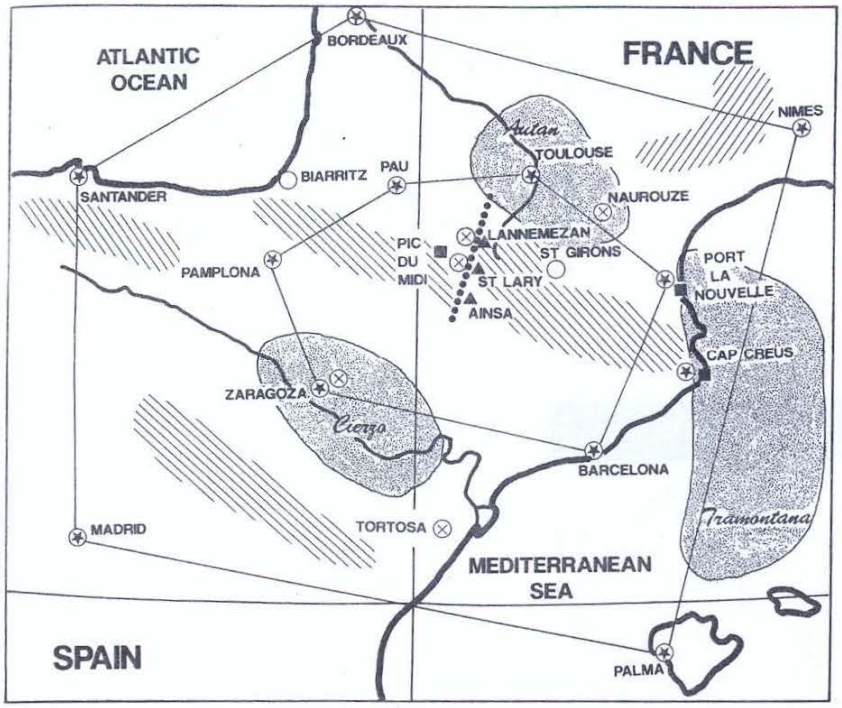

Fig. 1. Synoptic view of the ground infrastructure during PYREX. The climatological range of the winds is indicated by half-tone. ⊛ Soundings; ▲ profilers; ⊗ sodar; ● microbarographs; ■ constant level balloons

Table 2. A list of the facilities operating during PYREX

Instrument	Location	Responsible institute
15 auto stations	Central transect	CNRM
3 auto stations	Naurouze, ...	EDF
2 sodars	Naurouze, Saint Lary	EDF
Sodar	Lannemezan	CRPE
Sodar	Zaragoza	INM
Sodar	Tortosa	UV
VHF profiler	Lannemezan	LSEET
VHF profiler	Saint-Lary	CNRM
VHF profiler	Ainsa	LAMP
UHF profiler	Lannemezan	CRPE
Balloons	Pic du Midi Port la Nouvelle Cap Creus	LA, CNRM and CNES
Falcon 20		DLR
Fokker 27 ARAT		CNES, INSU, Météo-France, IGN
Piper Aztec		CNRM
Merlin IV		CNRM

vation of additional upper-air soundings, and to the intensification of basic measurements. The IOPs centered in time around aircraft operations. The aircraft flight plans were organized depending on specific missions. There were four different mission types, corresponding to the documentation of the main mountain wave/lee wave system, and to the documentation of the mean flow and turbulence in either of the three regional winds caused by the Pyrénées: Autan, Tramontana, and Cierzo. The climatological ranges of these winds are shown in Fig. 1. During the 2 months duration of the experiment, (October and November 1990) we encountered good climatic conditions for all four types of missions. There were 10 IOPs totalling 15 days of intensive measurements. A summary of the IOPs starting and finishing times, types of event, and aircraft/balloons operations is given in Table 3.

2.1 Permanent surface networks

The location of the regularly operating surface stations of the area of interest is shown in Fig. 2. They include different types, ranging from the main stations of the WMO network, regularly staffed and operating continuously, to stations of local interest, and a large number of fully automated stations. In fact, the PYREX area is probably one of the most densely covered in the world by surface meteorological measurements, which made it an ideal candidate for such a field study. However, some gaps were noted in the permanent network, which justified the installation of three additional surface stations by EDF on the Pyrenean foothills. During the field phase all stations operated as usual, generating a large diversity in the periodicity, nature and format of their measurements. In order to ease further interpretation work, the format and periodicity of all the data sources have been normalized in the Pyrex data base. Most data are available on a half hourly basis. All stations reported temperature, humidity, wind strength and direction, and several of them reported pressure. For most of these, the pressure sensors had been specially visited and calibrated just before the beginning of the experiment. In addition, a large number of stations reported on wind gust speed and direction, rainfall, radi-

Table 3. List of IOPs and operations

POI	Start MMDDHH	End MMDDHH	Synoptic wind	Operations	Comments
1	100418	100518	north	1 Piper flight Tramontana 1 Merlin flight Tramontana Balloons Port la Nouvelle	
2	101118	101406	south	2 Piper flights Autan 1 Fokker flight Autan 1 Merlin flight Autan	
			south	1 Fokker central transect flight 1 Merlin central transect flight Balloons Pic du Midi Balloons Cap Creus Sailplanes	
3	101418	101512	south	1 Piper flight Autan 1 Merlin flight central transect 1 Fokker flight central transect 1 Falcon flight central transect Balloons Pic du Midi Sailplanes	Best case of lee waves from south
4	102018	102118	south	1 Piper flight Autan 1 Merlin flight central transect 1 Fokker flight central transect Balloons Pic du Midi Balloons Cap Creus Sailplanes	
5	102518	102612	south	1 Piper flight Autan 1 short Merlin flight Balloons Cap Creus	Front crossing the area during operations
6	110318	110518	north	1 Piper flight Tramontana 2 Merlin flights Tramontana 2 Fokker flights Tramontana Balloons Cap Creus	Tramontana weakens during 2nd day
7	110618	110718	south	1 Piper flight Autan 1 Merlin flight Autan 1 Fokker flight Autan Balloons Cap Creus	
8	111118	111218	north	1 Piper flight Cierzo 1 Merlin flight central transect Balloons Cap Creus	
9	111406	111618	north	2 flights Piper Tramontana 3 Merlin flights central transect 3 Fokker flights central transect 3 Falcon flights central transect Balloons Port la Nouvelle	Best case of lee waves from north Strongest Tramontana
10	112818	113018	north	2 Piper flights cierzo 2 Merlin flights cierzo 2 Fokker flights cierzo Balloons Port la Nouvelle	Best Cierzo on 2nd day

ation, and weather conditions. All this information has been kept in the data base to facilitate the interpretation. A quick-look atlas of these surface measurements, containing a discussion of the validation procedures, has been prepared by Champeaux and Péris (1991).

2.2 CNRM portable network and drag computation

An extra network of 15 automated surface stations was operated by CNRM during the field phase. Those stations have been installed at selected mountain sites of known altitudes, along a transect perpendicular to the main range, as shown in Fig. 3. This will be called in the following the central transect. In addition to the usual meteorological observations, high quality pressure measurements were made at these stations, in order to determine the pressure drag across the range. A quick-look atlas of these data has been prepared by Puech *et al.* (1991).

From experience gained during ALPEX (Richner, 1987), the absolute accuracy requirements for pressure

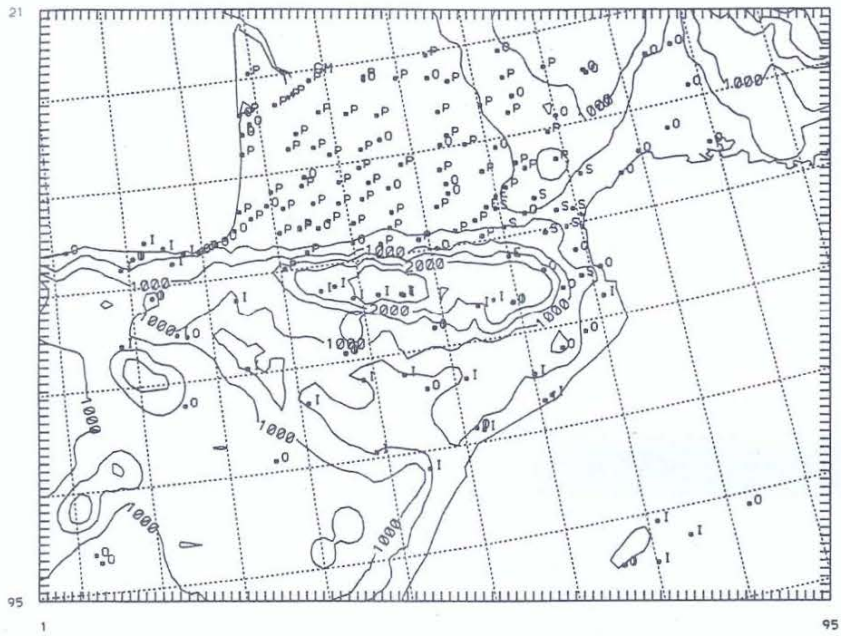

Fig. 2. The permanent surface networks operating during PYREX. The letters denote the different networks that have been blended in the PYREX data base. O indicates regular WMO stations, P stations of the PATAC network (south-west France), S stations of the departmental networks of Aude and Pyrénées Orientales (France), E stations specially installed by EDF, and I network of automated stations of the INM

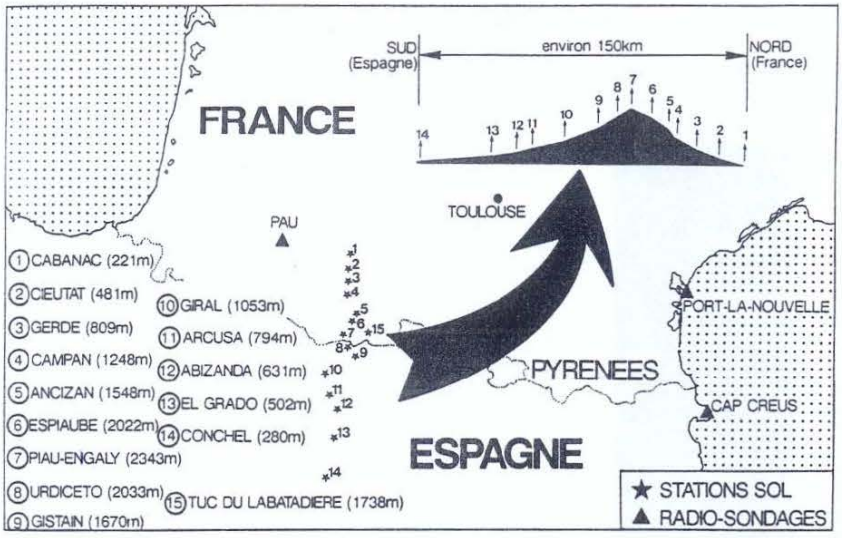

Fig. 3. The situation of the CNRM portable network (from Puech *et al.*, 1991)

measurements was thought to be of the order of 0.5 h Pa and 0.2 h Pa for relative accuracy. This accuracy was attained by taking the following precautions: high quality sensors were used, dynamic effects due to the wind were eliminated, pressure and temperature corrections were made, and the altitudes of the stations were known to better than 10 cm. Also, the locations and altitudes of these stations had been selected to be as close as possible to the averaged terrain elevation for the same distance from the crestline. Thus, the network provided an adequate sampling of the mountain profile (see Fig. 3). The Davies and Phillips (1985) procedure was used to compute the drag per unit area every 10 min (units Pa) by the formula

$$D = L^{-1} \int_{z_{\text{bottom}}}^{z_{\text{top}}} \Delta p\,(z)\,\mathrm{d}z\,,$$

where $\Delta p(z)$ is the pressure difference between the two mountain sides at height z, retrieved from the raw data by spline interpolation, and L the length of the instrumented transect. By convention, Δp is positive when the pressure is higher on the northern side of the range, i.e. for northerly synoptic flow. This method was chosen because it operates with the observed pressure only (no reduction of the pressure to a standard level), and takes full advantage of the good relative accuracy of the sensors. Since the Pyrenean range is roughly two-dimensional, this value is thought to be representative of the pressure drag in the direction of the main transect in the central part of the mountains. It is probably higher than the pressure drag per unit area on the whole of the mountain range, and gives no information on the pressure drag in the direction parallel to the range (i.e. perpendicular to the transect).

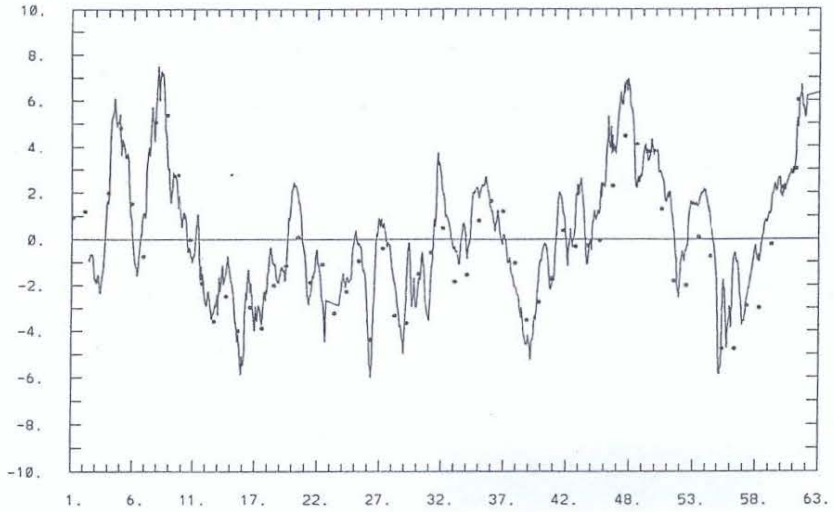

Fig. 4. The 2 months time series of the surface pressure drag computed from measurements of the CNRM portable network (continuous thin line). The SLP difference between Pau and Zaragoza is shown as symbols. The abscissa is in days, starting from 1 October 1990. The ordinate is to be understood as Pascals for the drag, and hPa for the SLP difference. (from Puech *et al.*, 1991)

Numerical modelling will be used to derive the correspondence between this observed value and other determinations of the drag (see Section 3.3).

During the field phase the pressure drag was computed as explained above in quasi-real time (every half hour, with a time resolution of 10 min), thanks to the data transmission via Météosat to the experiment headquarters in Toulouse. As a synthetic indicator of the situation it was used for most of the decisions concerning the special operations. After the experiment all computations were rerun with carefully qualified data. The resulting 2-month time series is shown in Fig. 4, which constitutes one of the major experimental results. The pressure drag, from Fig. 4, ranges from -7 to $+8$ Pa. Its algebraic mean value is 0.2 Pa, and its absolute mean value is 2.2 Pa. This indicates that the Pyrenean range is indeed a major sink of meridional momentum for the atmospheric flow. As expected, the time variations of the drag are very much correlated with the synoptic wind variations. We also found a weak diurnal cycle (0.4 Pa amplitude). The robustness of the drag estimate was evaluated from a sensitivity study, where every station was successively removed from the interpolation. This resulted in a change, usually less than 0.1 Pa, and in any case smaller than 0.5 Pa, confirming that the spatial resolution of the ground network was adequate to perform this drag computation. Previous results from Davies and Phillips (1985) with the ALPEX data showed a larger sensitivity to removing from Davies and Phillips (1985) with the ALPEX data showed a larger sensitivity to removing some stations from the computations.

Finally, an effort to cross-validate the present drag estimate with other data sources has been undertaken. For instance, the correlation with the difference between the sea level pressure (SLP) at two stations across the range (Pau, France, and Zaragoza, Spain) has been examined. Neither of these have been used in the previous drag estimate, which relies only on the measurements of the CNRM portable network. As is clearly shown by Fig. 4, the correlation is very good. Although in principle such correlation was strongly expected, here it reaches a very high level (the correlation coefficient is 0.91), and extends to very small details of the curves. This means that such details are not computation artefacts, but contain real information on the drag fluctuations, that will therefore need interpretation in terms of the synoptic, or meso-scale situation. This reinforces our confidence in the quality of the data set. Finally, the most simple regression suggested by Fig. 4, reads

$$D = 0.01\,(SLP_{\text{Pau}} - SLP_{\text{Zaragoza}})\,,$$

where units are Pa throughout. This empirical formula may be used in the future with a high degree of confidence to deduce the Pyrenean drag from routine measurements. Furthermore, the high density of stations along the central transect has allowed us to study the vertical distribution of the contribution to the drag, and a variety of factors influencing the drag. For instance, the correlation coefficient between the drag and the temperature difference from side to side is found to be 0.78.

2.3 Upper air soundings

For the purpose of the experiment, the regular sounding network was upgraded to 12 sites in the PYREX area (see Fig. 1). The soundings were organized in two arrays. The outer array is convenient to estimate meso-alpha-scale quantities, whereas the inner array, composed of stations in the immediate vicinity of the range, is convenient to sample the meso-beta-scale features of the orographic influence. Soundings of the inner array are kept in the data base with the maximum available vertical resolution, whereas for those of the outer array, we have retained the significant and standard levels only. The soundings were not activated outside the Intensive Observation Periods (IOPs), except for the normal operation of the WMO network. During the IOPs, they were made at 00, 06, 12, and 18 GMT. Most of these soundings were transmitted in real time via the meteorological transmission network, and entered the assimilation cycle of the Météo-France

operational forecasting system. The total number of soundings received, validated, and archived into the PYREX data base is 720.

2.4 *Acoustic sounders*

Five acoustic sounding systems (sodars) were implemented continuously during the experiment at 15 min time resolution (see Fig. 1). Some of them were located at places adequate to follow the Cierzo and Autan wind evolutions. Others were colocated with the profilers on the main transect, at places of interest to document the ground manifestation of the mountain waves. The sodars provided measurements of the low-level wind profiles, nominally from about 50–500 m above the instrument. However, the performances were in general inferior when the wind was strong, because of the increase in antenna noise. For technical reasons, the data of the Tortosa sodar are not usable. Carissimo *et al.* (1991) contains some quick-look data from the two sodars operated by EDF.

2.5 *Wind profilers*

Four profilers of the Météo-France/INSU research network were operating continuously during the experiment. They were located on three sites along the main transect, on either side of the range and very close to the crest. The north side (Centre de Recherches Atmosphériques at Lannemezan) had two colocated profilers, covering different ranges of altitudes, namely a UHF radar (Petitdidier *et al.*, 1990), ranging from 1000–6000 m with 150 m vertical resolution, and a VHF radar (Crochet, 1983), ranging from 1500–18 000 m with 750 m vertical resolution. The two other sites had more recent instruments with an ability to cover various ranges of altitudes, depending on the operating mode (three modes were available, low resolution, high-resolution, and coded mode, a special feature improving the range). The nominal requirements for these instruments called for profiles vertical resolutions of 375 m (up to 12 km) and 2250 m (up to 18 km). Those were generally not attained, because the profilers were prototype research instruments, with limited power. As a consequence, the measurements were often limited by ground clutter and by several technical problems. We have decided to retain formally in the data base in the nominal and space resolutions during the IOPs, and to assign to each data a quality code varying from 0–8, depending on the signal/noise ratio. The data are also available outside the IOPs at a time resolution of 1 h. The performance of the profilers vary widely from day to day and from site to site, but despite the above-mentioned problems, much valuable data was gathered and we plan to perform several model/profilers and pressure drag/profilers comparisons.

2.6 *Constant level balloons*

The constant-level balloons described by Benech *et al.* (1987) were operated to obtain air trajectories, and in situ measurements of pressure, temperature and moisture. Three launching sites were used (Fig. 1). One at Pic du Midi (close to the highest point of the central transect) was operated in case of lee waves on the northern side of the range. The balloons from this site were tracked by a radar in Lannemezan. Their nominal flight height ranged from 3000–5000 m. Two other sites at Port la Nouvelle (France) and Cap Creus (Spain), on the eastern side of the range, were used to obtain low-level trajectories (400–1500 m height above sea level) in the flow deviated laterally by the range. The plans called for the use of the northern (southern) launching site for northerly (southerly) flows, and to track the balloons from both sites successively via the Loran C localisation system. Some technical problems rendered this optimal situation impossible during part of the experiment, but a large number of balloons have been tracked during the IOPs. Trajectories tracked from one reception site are usually about 100 km long, while trajectories reconstituted from both reception sites (the optimal situation) reached 200 km in several cases, which is well beyond the present day expectations for such an experiment. Generally speaking, the balloon experiment was very successful, and provided reference data for the wind and the air-mass trajectories, which are very useful to assess the value of other types of measurements. The balloon data have been summarized by Koffi *et al.* (1991 a, 1991 b).

2.7 *Aircraft measurements*

Four research airplanes have been used for PYREX missions. These are the Fokker 27 ARAT (Avion de Recherche Atmosphérique et de Télédétection), operated by a group of French institutes (CNES, INSU, Météo-France, and IGN, see list of acronyms), the Merlin IV and the Piper-Aztec of Météo-France, and the Falcon 20 of DLR. The Fokker, Merlin, and Falcon aircraft performed both turbulence and mean flow measurements, while the Piper measured only mean flow parameters. Besides wind, temperature, and moisture, which were the most needed measurements, additional measurements were made: radiation in most cases, microphysics for the Merlin and Fokker, and lidar for the Fokker (see below). There were two intercomparison flights between the French airplanes during the experiment. These flights helped to resolve small discrepancies between the measurements, and to prepare a synthetic aircraft data set, now available in the data base in a unified format. Three types of data may be used: (i) 10 s averaged data for all parameters and all flights; (ii) 1 s data for all parameters, restricted to the flight legs above the central transect (for a more detailed documentation of the lee waves); (iii) elaborate turbulence quantities computed from high frequency data for several flight legs (for comparison with model parameterization results).

The flight plans had been coordinated in advance with the air control authorities, who provided much help to re-route commercial traffic from the track of the research aircraft (especially for the central transect high levels, where there is significant traffic between France and

Spain). They were organized in missions focusing on one or other of the experimental objectives. The Autan mission called for the Merlin, Fokker, and Piper to execute coordinated flights in the geographical area of this wind. The Tramontana and Cierzo missions were fairly comparable, but in different geographical locations. These flights focused on detailed mean flow and turbulence measurements at three levels inside the atmospheric boundary layer (ABL), allowing for an overpass of the area with the lidar scanning down to explore the top of the ABL. The aim was to obtain accurate measurements of turbulence, and to interpret it in connection with possible organized structures (see Sect. 4 below). In these three types of missions, there were no high altitude measurements, and the Falcon was not used. On the other hand, the central transect mission called for the Falcon joining the Fokker and Merlin in a coordinated flight above the mountain, while the Piper was executing the same flight as in the other three missions, depending on the situation. The Fokker and Falcon crossed the main range several times, flying right over the CNRM portable network, while the Merlin was assigned a fairly complicated flight plan, made of legs parallel to the main range at different elevations and distances from the crest. The pilots had been asked to fly as low as it was reasonably possible to try to document the ABL over a higher mountain. However, the turbulence level encountered in these flights was usually very low, indicating that the mountain ABL is very shallow. Another objective of this flight pattern was to assess the variability of the flow along the range and to study how the 3D perturbations created by individual peaks are smoothed out in altitude to generate a simpler, 2D pattern. We believe that, despite the low turbulence, this data set is one of the most original ever acquired over a mountainous area, and opens interesting opportunities to derive the effective mountain roughness, via indirect methods (in comparison with model predicted winds, for instance). The Fokker and Falcon flights were more classical, and will be used to compute the wave momentum fluxes. The list of the available flights is given in Table 3. The flight logs of the on-board scientists have been published by Attié *et al.* (1991). Note that the flight plans were fairly detailed, as a consequence of previous knowledge of the flow, and that the flights were fairly repetitive. This resulted in more comparable sets of data from one flight to the other. Indeed, we wanted to assess how slightly different synoptic situations can affect the mesoscale patterns, without introducing flight differences into the interpretation.

2.8 Airborne lidar

Perhaps the most novel aspect of PYREX was the use of an airborne lidar. A new backscatter lidar has been developed by CNRS (SA, LMD, and INSU) in the framework of the LEANDRE research program (Pelon *et al.*, 1990). It had been tested on board the Fokker in autumn 1989 and spring 1990, and was involved in its first cooperative campaign during PYREX. Lidar measurements could be made both in the direction of zenith and nadir from the Fokker aircraft. They provided complementary observations of the perturbations induced by orography, as shown by tracers such as particles and clouds. The top of the ABL is also easily detected by such measurements, and is a very useful quantity for the interpretation of in situ measurements. Lidar measurements were performed during most Fokker flights, and some examples will be discussed below.

2.9 The PYREX data base

A significant effort has been made to integrate the previously described data sets into a unified data base, allowing for an easy access to the interested scientists. An interactive, relational system has been used. The principles of data access and organization are discussed by Bougeault and Benoit (1992), where a large number of examples are also given. The PYREX data base contains much information in addition to the measurements discussed above. For instance, we have included the Météosat and AVHRR visible and infrared pictures of the area during the IOPs. Also available are the analyses of the mesoscale operational model Péridot of Météo-France (Bougeault and Mercusot, 1992), which are specifically designed to initialise simulations of research models.

Finally, some additional measurements are available on a non-systematic basis. At the request of Météo-France and INM, several commercial aircraft companies have made special reports of the wind during the field phase, and have provided the project group with these observations. Data from several ship reports, and some buoys in the western Mediterranean have also been included in the data base. Cooperation was established between the project group, the Fédération Française de Vol à Voile and the French Airforce authorities. Three civilian and military sailplanes, based in Saint-Girons, (France) participated in the PYREX operations when the weather permitted, and qualitatively documented the lee wave system. The objective of this operation was to ascertain the 2D nature of the lee wave system, which was thought to be possible with the qualitative measurements available on board the sailplanes. In one case (IOP3, see below), this cooperation resulted in scientifically useful results. But another, more difficult to quantify, benefit of this cooperation, relies in the qualitative appraisal of the PYREX situations by the sailplanes pilots. Indeed, what we scientists, consider as our best southern case (IOP3), turns out to be a rather common, medium strength situation for the pilots, who had used the Pyrenean lee waves for their fun all year round for many years. This puts in a climatological perspective the conclusions that may be drawn from the PYREX data on the dynamical impact of the mountain.

3 An example of strong mountain wave/lee wave system: IOP3

In this section, we shall try to illustrate the complementarity of the various observation means on one of the best

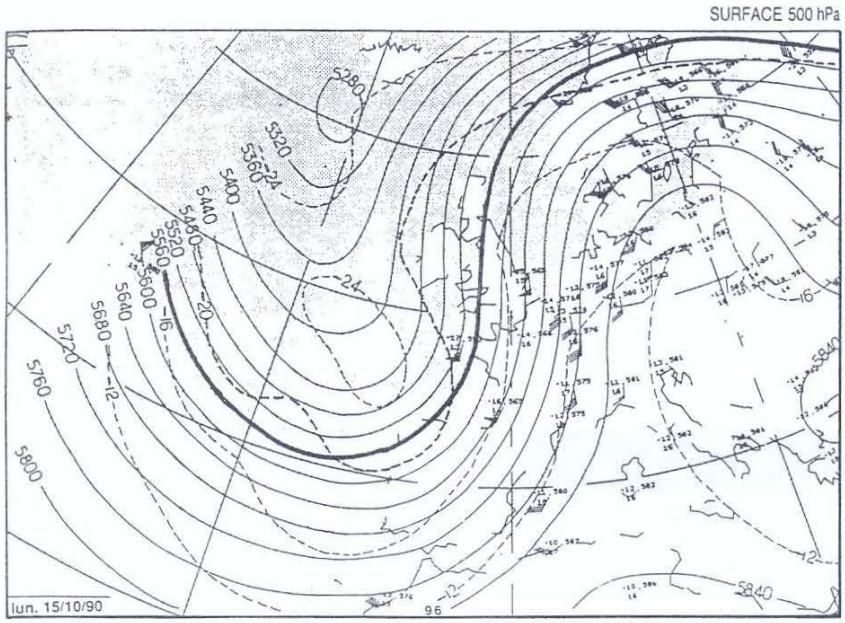

Fig. 5. The 500 hPa chart of 15 October, 1990, 1200 GMT. *Continuous lines* stand for the geopotential height, *dashed lines* stand for the temperature (Celsius)

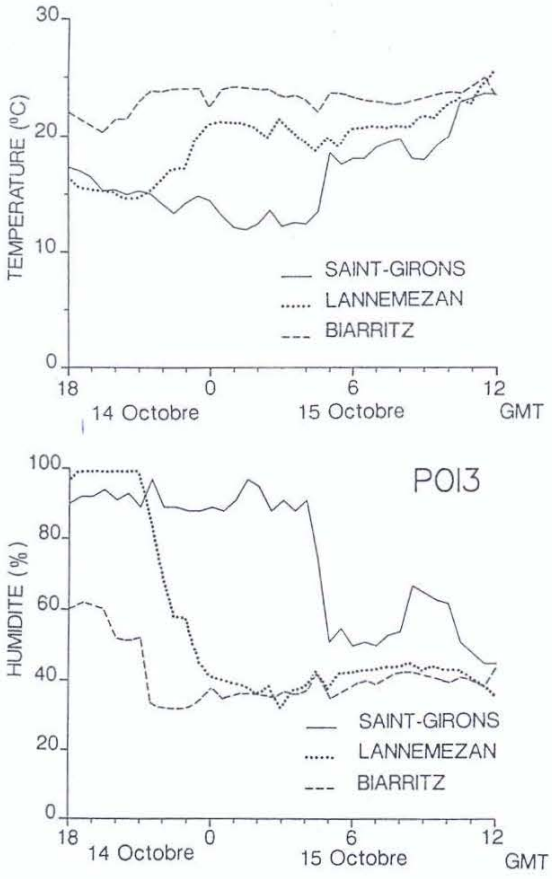

Fig. 6. Time sequences of temperature and humidity at three stations of the Pyrenean foothills (Biarritz, Lannemezan and Saint-Girons), showing the foehn onset progressing from the west to the east during the night from 14 to 15 October, 1990 (from Champeaux and Péris, 1991)

PYREX situations, the 3rd IOP, that extended from 1800 GMT 14 October to 1200 GMT 15 October, culminating with the aircraft mission, from 0600–1000 GMT. The synoptic situation (Fig. 5) was dominated by a deep trough extending over the eastern Atlantic Ocean, resulting in a south to southwesterly flow over Spain and France at all levels above 800 hPa. The whole system was drifting slowly towards the east, and the wind did accelerate steadily during the night, reaching a maximum in the morning of 15th October, just after the aircraft mission. The speed was then about 15 m s^{-1} at 700 hPa, 20 m s^{-1} at 500 hPa, and 40 m s^{-1} at the tropopause, just above 200 hPa. The airmass hitting the range was rather moist, resulting in low-level clouds upstream of the mountain, and alto-stratus formation downstream. It was separated from a drier airmass to the west by a weak, undulating front, that reached the western edge of the Pyrenean range at 1200 GMT, 15 October.

3.1 Meso-beta scale aspects: foehn, autan and mountain wave

In this fairly typical situation, the foehn effect started during the night on the northern side of the range, consecutive to the increase in the synoptic wind. The foehn onset may be seen spectacularly in the temperature and humidity sequences from several stations in the foothills (Fig. 6). It follows more or less the eastward drift of the system: The first temperature rise occurs in Biarritz (at the western edge of the range) between 2000 and 2130 GMT. This is followed by several stations in the central part of the range between 2330 and 0030 GMT, and the effects propagates to the north between 0100 and 0200 GMT. Finally, the eastern part of the range is also reached by the foehn effect between 0400 and 0500 GMT. This is accompanied

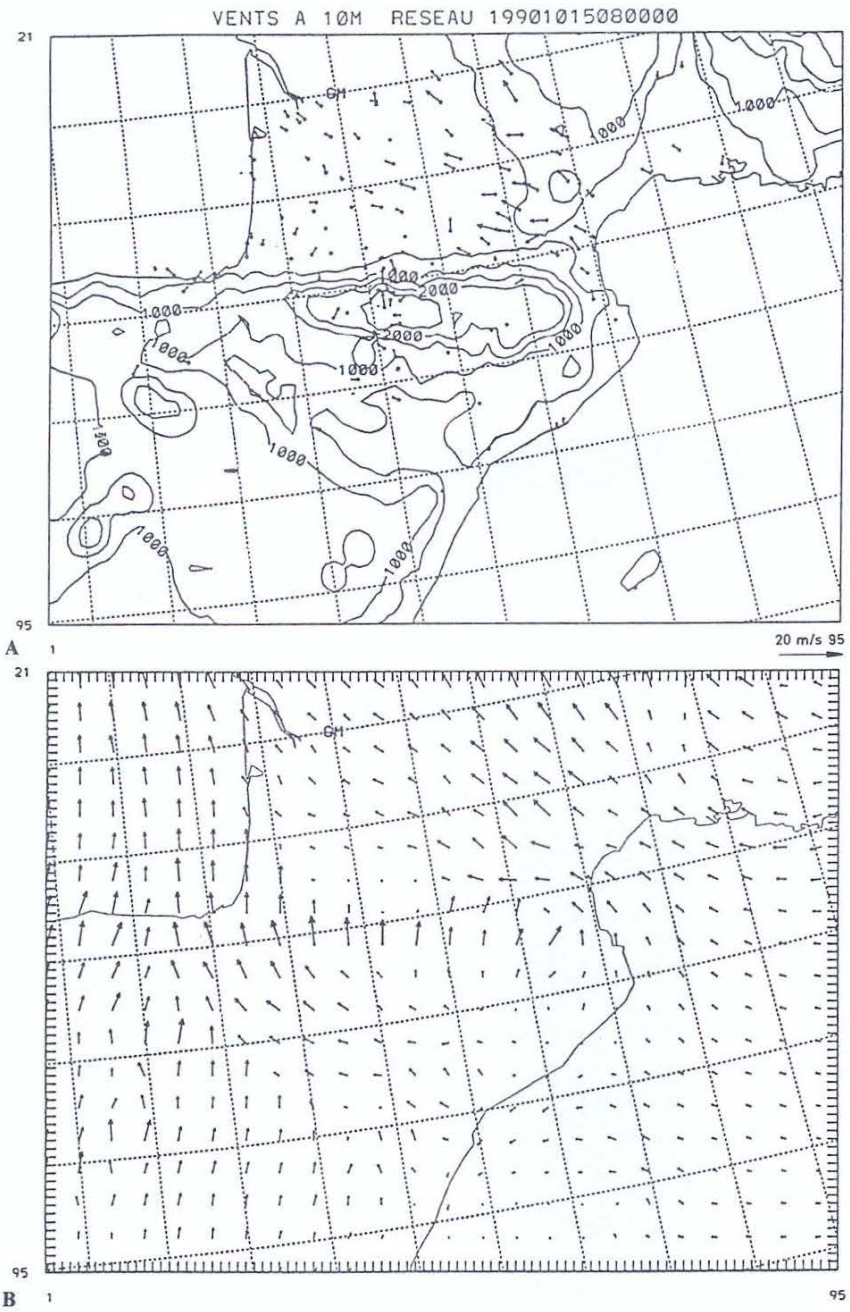

Fig. 7 A, B. Surface (10 m level) winds **A** observed in the area at 0800 GMT, 15 October; **B** simulated by the Péridot meso-scale model of Météo-France

nearly everywhere by drying and southerly wind (not shown). The maximum wind gust observed is 16 m s^{-1} from south, in Lannemezan (Central Pyrénées). At sunrise on 15 October, the temperatures reached 18 °C in all of south-west France, and more than 20 °C in the foothills, an unusually high value for the season.

During the aircraft mission (morning of the 15th), there was not much change in this situation. A general view of the surface wind at 0800 GMT (Fig. 7A) shows that the PYREX area is divided into several well-identified subdomains. The northern foothills are under the influence of the foehn, with southerly winds reaching 10 m s^{-1} in the central part. Going to the north, we find an area of weak and disorganized winds, which corresponds well with climatological wind speed minimum in this area, usually referred to as the "sheltering effect" of the range (although the origin of this weak wind is certainly more complicated than a mere sheltering effect, it is obvious that the occurrence of weak winds at this place is caused by the presence of the mountain). Moving to the east, one enters the domain of the Autan wind. The wind starts, as usual upstream of the Naurouze path, accelerates in the diffluent vane created by the slopes of Pyrénées and Massif Central, and extends to the Gers hills to the

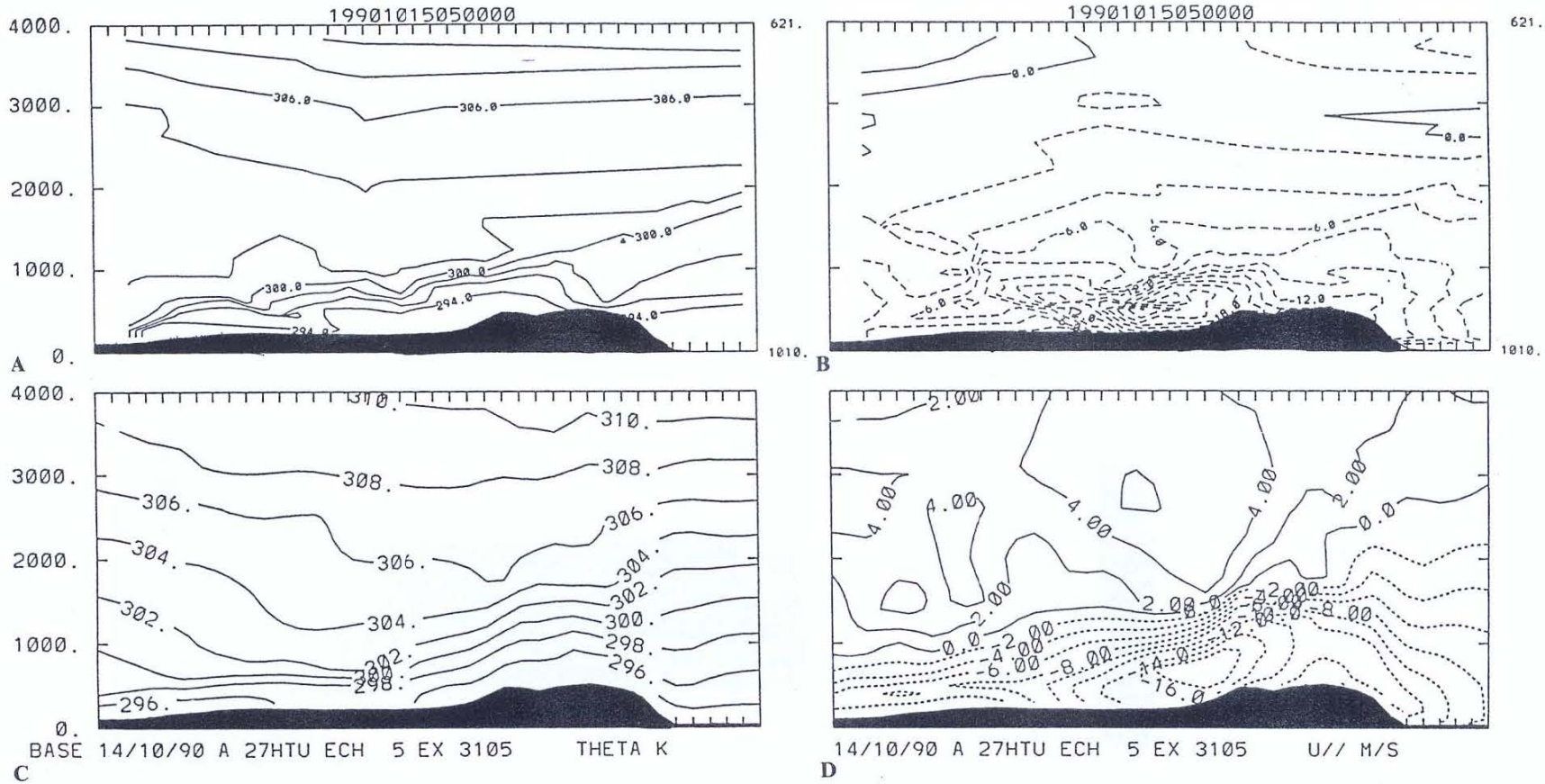

Fig. 8A–D. Vertical cross-sections along the Autan wind principal axis. **A** Potential temperature interpolated from measurements of soundings in Port La Nouvelle, Toulouse, and Pau, and of the Piper flight. **B** Wind component parallel to the cross-section, interpolated from the same data sources. **C** Potential temperature simulated by the Péridot model. **D** Wind simulated by the Péridot model. The western side is on the left side of all pictures, and the marks on the x axes stand for the grid points of the model, which are spaced by about 10 km

west. The maximum intensity is seen to occur on the southern slopes of the Massif Central and reaches 15 m s^{-1} with 20 m s^{-1} instantaneous gusts reported. This is confirmed by the Naurouze sodar, which measured 15 m s^{-1} surface wind, increasing to 25 m s^{-1} at 400 m above ground. It will be interesting to study which part of the wind is caused by the Pyrénées alone, and which part is due to the channelling between the two mountain ranges. Further to the west, southerly winds in agreement with the upper level flow are observed. Finally, on the upstream side, the flow is clearly channelled into the Ebro valley, leading to a southeasterly wind directed towards the western edge of the Pyrénées. That feature may explain why the foehn is in general stronger on the western side of the Pyrénées and on the nearby Pays Basque.

On 15th October the Piper aircraft performed one of its 6 autan flights. The flight plan called for oblique soundings between Toulouse and the Mediterranean coast, to document the depth of this shallow wind layer. These measurements have been processed, together with the nearby soundings, to produce the synthetic wind and temperature cross-sections shown in Fig. 8 A, B. They depict a 20 m s^{-1} easterly wind, extending from the surface to 1000 m above sea level, capped by a strong temperature inversion. Note that the inversion is not present in the upstream part, probably meaning that it is generated by dynamical processes forced by the orography.

The main mountain wave was studied using the Falcon and Fokker flights above the central transect to construct synthetic cross-sections of several parameters. The method used was fairly simple. It assumed that the flow was stationary, averaged the raw data over 10 km along the flight tracks and interpolated between these averaged data in the 2-D vertical plane. Thus, lee waves are filtered (see next section for a lee wave discussion), and only the main mountain wave remains. The Fokker legs used had an altitude of 4000, 4400, 5000, and 6000 m above sea level, and were flown between 0602 and 1016 GMT. The Falcon legs were at 8200, 9400, 10 000, 10 600, 11 200, and 11 800 m above sea level and were flown between 0558 and 0820 GMT. Since the synoptic wind was still slightly increasing during that period, the effects of unstationarity will need a careful study in forthcoming work. The potential temperature and humidity cross-sections obtained by this method (Fig. 9) nevertheless show a well established mountain wave, extending up to the lower stratosphere, with a slow phase reversal in the troposphere, and a weak, but definite, upstream tilt. One may therefore expect a negative associated momentum flux, as shown below. The less pronounced wave amplitude at 7000 m above sea level is in agreement with the profiler observations of the lee waves (see below). Note, however, that it may also be due to the absence of aircraft data at this height.

The case has been modelled with the research version of the Péridot French Weather Service operational limited area model. The model is based on the hydrostatic, primitive equation system. It uses a terrain-following, sigma vertical coordinate and has a fairly detailed physical package. It has been validated for similar types of flows by Bougeault and Lacarrère (1989) and Stein (1992). We

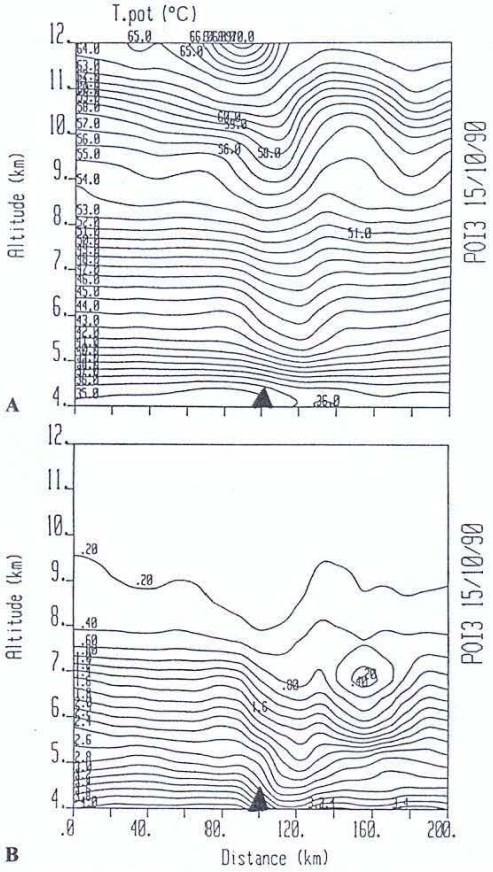

Fig. 9 A, B. Vertical cross-sections along the central transect, obtained by interpolation of measurements of the Fokker and Falcon flights (south on the left side). **A** Potential temperature (Celsius). **B** Mixing ratio (g/kg)

used a 10 km horizontal mesh over a domain of 95 × 95 grid points centered on the Pyrénées, in polar stereographic projection, and a vertical grid of 30 levels regularly spaced by 500 m, with increased resolution in the low levels. This allows to capture the meso-beta scale details of orographic flows. The topography was prepared from a 1 km resolution geographic file, and used an envelope orography formulation reaching 2900 m, comparable to the averaged height of the main crestline in the central part of the Pyrénées. The model is initialized and forced on the boundaries by the meso-alpha-scale analyses interpolated from the grid of the operational model (35 km mesh). Note that the assimilation cycle of this model had been rerun with all available upper-air soundings. This procedure ensures that the initial condition of the research model contains no small-scale features. All such features are created subsequently by the model as part of an adjustment to the small-scale orography. The run presented here started at 0300 GMT and ended at 1200 GMT. The results agree reasonably well with the observations concerning the meso-alpha-scale patterns (altitude winds away from the mountain, general prediction, etc.), which is not surprising for this very short-term forecast, and is entirely due to the good quality of the

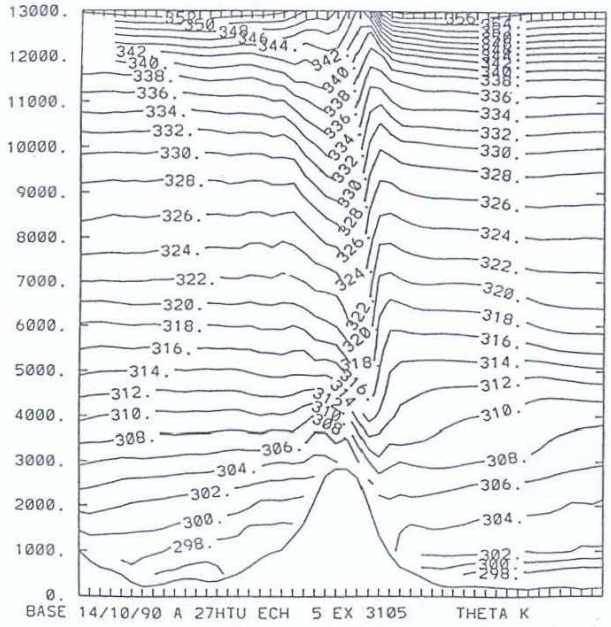

Fig. 10. Vertical cross-section of potential temperature simulated by the Péridot model along the central transect (south on the left side, and the marks on the bottom axis are spaced by 10 km)

Fig. 11. Picture obtained from NOAA11 visible channel on 15 October, 1417 GMT

initial condition. The discussion will therefore focus on the meso-beta-scale aspects. The surface wind predicted at 0800 GMT is shown in Fig. 7b, and may be directly compared with the observations in Fig. 7A. The different areas identified in the previous discussion are well reproduced. The autan cross-section (Fig. 8C, D) reveals that the model slightly underestimates the maximum wind speed. It also underestimates the strength of the inversion, perhaps because of insufficient vertical resolution. According to the hydraulic theory for downslope windstorms, these two problems are connected, and further experiments will be conducted with increased vertical resolution. The mountain wave itself is fairly well simulated as shown by the vertical cross-section in Fig. 10, to be compared to Fig. 9. On this picture, the foehn effect is also obvious. The overall quality of the simulation is therefore quite good, showing the capacity of such a model to capture the main features of the flow, if correctly initialized. These model results are used in Sect. 3.3 below to compute momentum budgets.

3.2 Meso-gamma scale aspects: the lee waves

As usual in such a case, lee waves were excited downstream of the range. These waves were topped by cloud bands, visible from the ground during most of the day. They can be seen on the NOAA11 AVHRR 1417 GMT visible image in Fig. 11. It is unfortunate that earlier satellite images of that day cannot give any information on the lee waves during the aircraft mission because of the higher level cloud cover. The lee wave event of IOP 3 has been described by Bénech *et al.* (1993). They showed that the horizontal wavelength of these waves was about 10 km around 0700 GMT, with some variations with the altitude, in agreement with the wavelength one would deduce from the Scorer parameter structure computed from the Zaragoza (upstream) sounding for 0600 GMT. The lee waves could be documented by the aircraft, the balloons, the sailplanes, the lidar, the profilers, and had also low level manifestation, as shown by the sodar data. A synoptic view of the vertical velocity measurements by the Falcon, the Fokker, and the three constant level balloons released from the Pic du Midi is shown in Fig. 12. The vertical velocity reaches a maximum amplitude of 6 m s^{-1} in the altitude range 3500–6000 m, and decreases at higher altitudes. Some activity is also noticed around 10 000 m. It should be remembered that the situation was not perfectly stationary, and that these measurements are not simultaneous, but cover about 4 h in time.

Because of the slow time variation of the mean flow, the waves were not stationary with respect of the ground. The LSEET VHF profiler in Lannemezan was ideally situated to observe this time drift. The time evolution of the vertical velocity profile from this instrument is shown in Fig. 13. It is noticeable that the strongest activity coincides with the results of aircraft measurements, with maxima below 6000 m and around 10 000 m. The maximum amplitude is found at 3750 m between 0500 and 0800 GMT, and reaches about 3 m s^{-1}. The period is best defined between 0600 and 0900 GMT, and is roughly 2 h. This phenomenon has also been observed by the CRPE UHF profiler, also present on the Lannemezan site (not shown). An approximate phase velocity of the lee waves with respect to the ground can be deduced by dividing the wavelength by the observed time frequency, resulting in the value 1.3 m s^{-1}.

The third instrument located in Lannemezan was the CRPE Sodar. It observed south-easterly wind of about

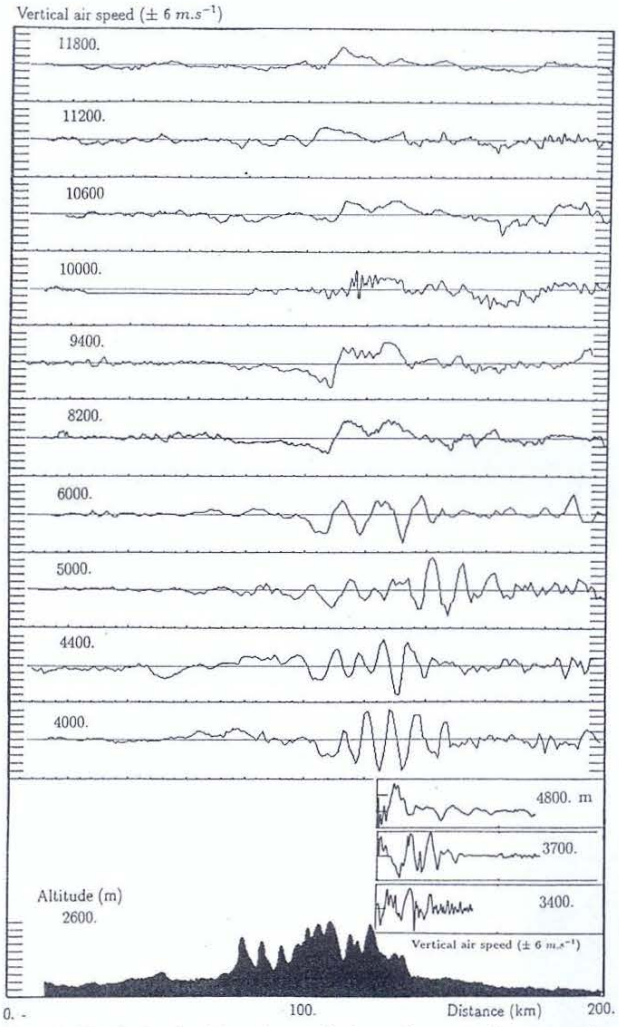

Fig. 12. Vertical velocities observed along the central transect by the constant level balloons (*three lower curves*), the Fokker (*next four curves*), and the Falcon (*six upper curves*). The vertical scale is such that the total depth available for each of the curves between two horizontal lines goes from -6 to $+6$ m s^{-1}

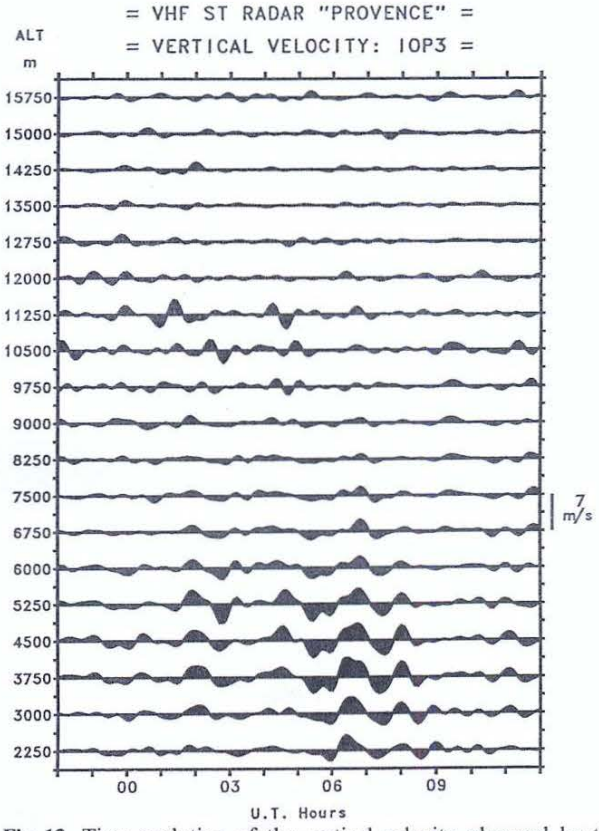

Fig. 13. Time evolution of the vertical velocity observed by the VHF profiler in Lannemezan. The scale is indicated to the right of the picture. The vertical velocities were obtained every 4 min 50 s. Each individual measurement is representative of a 750 m vertical window, and the horizontal window varies from 145 m at 2250 m to 1325 m at 15750 m. The mean error is estimated at 0.12 m s^{-1}. In order to remove the slow variations, and to reduce the noise, a band-pass FFT-filtering technique has been applied to the raw data, keeping only the time scale from 30 min to 3 h 30 min

7 m s^{-1} during the morning of 15 October. Some computations of the friction velocity have been performed directly from the high-resolution (4 s) independent velocity components measurements (Kotroni and Mazaudier, (1992). They show (Fig. 14) that the friction velocity oscillates between 0.4 and 0.6 m s^{-1}, superposed on a slow increase. The period of this oscillation, about 2.5 h, is in fair agreement with the apparent period of the lee waves observed by the two profiles. One may therefore conclude that the lee-wave system generated variations of the turbulent momentum transfer in the ABL. It is remarkable that those periodic oscillations are much more visible on the friction velocity than on the air velocity itself (as measured by the sodar).

The airborne LEANDRE lidar was operating during the Fokker flights of IOP 3. Figure 15 shows the vertical cross-section of the range corrected signal obtained from the surface up to an altitude of 10 km along the central transect. South of the Pyrénées, at latitudes lower than 42.5 N, the cloud structure appears horizontally stratified with different types of clouds, extending probably from near the ground up to the tropopause. Above the crest, the clouds totally disappear, and clear air is observed between 42.6 and 42.8 N, and from 4–12 km altitude. This corresponds to the subsidence noted in the composite potential temperature cross-section discussed at Fig. 9, and confirms the structure of the main mountain wave. The altostratus then reappears and seems thicker than upstream, as confirmed by the available satellite images. In the low levels (near 4000 m), small clouds are seen at the top of the lee waves. They look similar to the clouds seen on the satellite image some hours later.

The mission of the sailplanes was to verify the two-dimensionality of the lee-wave field. Two exploration boxes of 50 km × 40 km had been defined, to the west and to the east of the central transect. The third sailplane was supposed to explore longitudinally the wave field above the plain. The range of altitudes covered was 4000–5500 m. The objective was to estimate the strength and direction of the wind from instrument readings taken when the

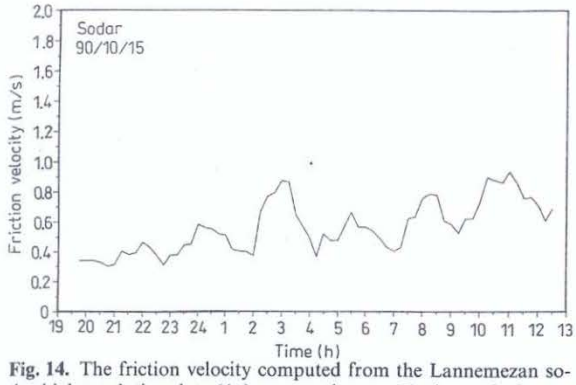

Fig. 14. The friction velocity computed from the Lannemezan sodar high resolution data (4 s), averaged every 15 min, at the lowest available measurement height (34 m)

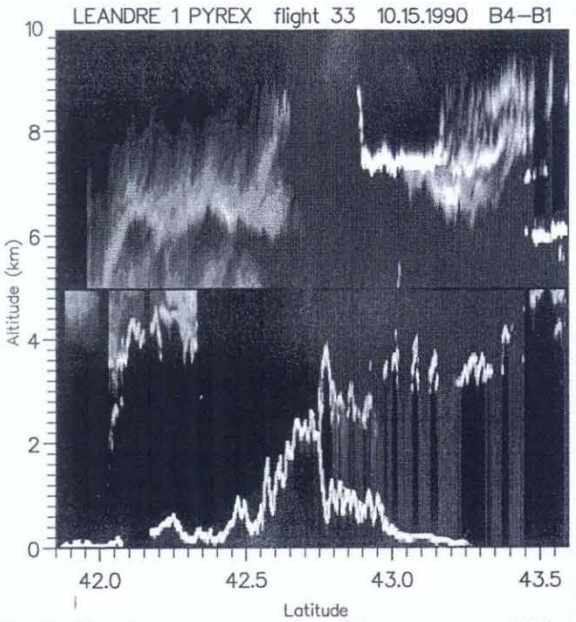

Fig. 15. Central transect cross-section of the range corrected lidar signal. This image has been reconstructed from two legs performed by the Fokker at 5700 m for nadir viewing, and at 4700 m for zenith viewing, between 0602 and 0727 GMT. The mountain shape is reproduced from clear-air lidar observations performed during another flight. Cloudy areas are characterized by high signal due to the cloud backscatter, reported on the figure as whiter pixels, whereas the clear air is represented as dark pixels. However, this distinction is not straightforward, and the transition from cloud to clear air is not easy to define, as no extinction correction is performed. As the lidar signal is rapidly attenuated through the cloud, the associated pixel brigthness is rapidly decreasing, which may suggest erroneous conclusions (for instance, clouds were actually observed above 7 km, upstream of the crest). This problem does not occur for the transition from clear air to cloud, which can be used accurately to describe the phenomena

sailplane was stationary (on the horizontal) with respect to the ground, and to note in this regime the readings of the variometer. These readings were later used to deduce the vertical airspeed by comparing the actual vertical velocity of the sailplanes and their theoretical vertical velocity. The results are summarized in Fig. 16, showing again the 4 well established lee waves. It seems that the waves were better organized at the east of the central transect, confirming an impression from the satellite picture. Thus, the quantitative measurements of the central transect could underestimate the event.

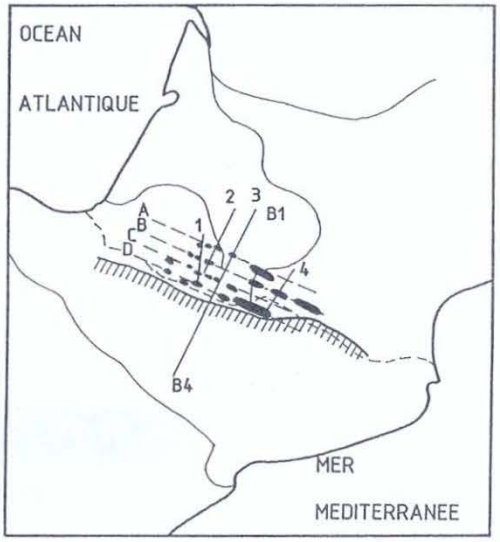

Fig. 16. Structure of the wave field deduced from the sailplanes observations. The observed zones of ascendence are *marked in black*. The axes of flight of the sailplanes (*lines A, B, C, D, 1 and 4*), of the airplanes (*3*), and of the constant level balloons (*2*) are given. The *hatched portion* is the region where clouds were blocked by the mountain. (from Bénech *et al.*, 1991).

The lee waves observed during IOP 3 have been simulated numerically by two 2D non-hydrostatic models. One model used is the non-hydrostatic numerical model Mercure, described by Buty *et al.* (1988). Simulations were carried out by Elkhalfi (1992) using the Zaragoza soundings at 0000, 0600 and 1200 GMT, 15 October. Moisture was not included, but may obviously play an important role that deserves further study. When using the 0600 sounding, the simulated wave length was approximately 13 km, comparable with the balloons and aircraft observations, but the model overestimated the wave amplitude above 4500 m. This may be due to the omission of the diabatic effects in upstream clouds (see Durran and Klemp, 1982), to insufficient surface friction, or to uncertainties in the upstream sounding. Finally, we cannot exclude the possibility that the mesurements have been taken in a place were the waves were less active than average (see above). With the two other soundings, the model response was similar at 0000 GMT, but weaker at 1200 GMT, in agreement with the observation (see e.g. Fig. 13, where the maximum lee-wave activity extends from 0300 to 0900 GMT). The model surface pressure drag has also been computed for all three cases, and was found generally smaller than the observation (Fig. 17). The hydrostatic version of the model is producing larger drag values, as expected from theory, which are closer to the measurements.

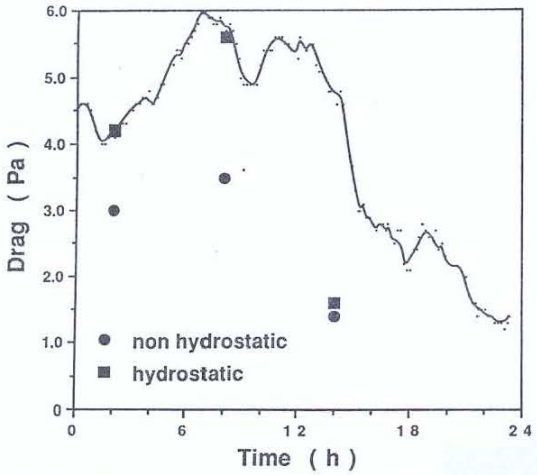

Fig. 17. The surface pressure drag measured during IOP 3, and the results of modelling by Elkhalfi (1992). Computations have been performed with the Zaragoza sounding at 0000, 0600, and 1200 GMT, and with both hydrostatic and non-hydrostatic versions of the model

The compressible model of Satomura (1989) has also been used (Satomura and Bougeault, 1992). The results of this model also exhibit strong lee waves, with amplitude larger than the observations (see Fig. 18 a). An interesting aspect of this simulation is shown in Fig. 18 b: the turbulence kinetic energy, computed here from a standard $k-\varepsilon$ scheme, shows a significant modulation by the lee waves down to the surface. This may help to interpret the sodar observations of the friction velocity presented above. Note that in these two models, the mountain shape was very smooth, and did not contain length scales comparable to the lee waves. It is therefore probable that these waves are generated by non-linear processes, as discussed by Durran (1992), among others.

3.3 An approach to the momentum budget

In this section, we will attempt to progress towards the central objective of the experiment by summarizing existing information on the momentum budget for this case. For brevity, we concentrate on the momentum component across the range, denoted ϱv. If we call u, v, w, the wind components, ϱ the air density, p the pressure, and f the Coriolis parameter, this equation reads

$$\partial_t(\delta v)+\partial_x(\varrho uv)+\partial_y(\varrho v^2)+\partial_z(\varrho wv)+\partial_y p+\varrho f u=0\,.$$

To volume average this budget in 3D boxes we define a vertical integration operator

$$\tilde{A}=\int_{h(x,y)}^{Z} A\,\mathrm{d}z\,,$$

where $h(x,y)$ is the local terrain height, and Z the (fixed) top of the integration box; and a horizontal averaging operator

$$\bar{A}=\frac{1}{\iint_\Omega \mathrm{d}x\,\mathrm{d}y}\iint_\Omega A\,\mathrm{d}x\,\mathrm{d}y\,,$$

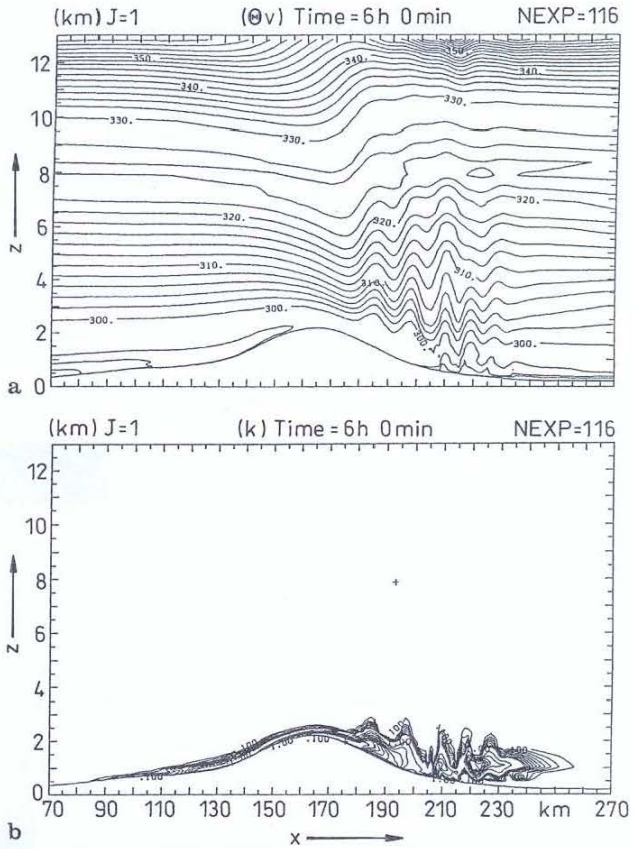

Fig. 18. Vertical cross-section of (**A**) potential temperature and (**B**) turbulence kinetic energy ($\mathrm{m^2\,s^{-2}}$) simulated with the model of Satomura (1989). The isoline interval is 0.1 $\mathrm{m^2\,s^{-2}}$.

where Ω is a horizontal domain. We apply these operators to the momentum equation, to obtain the Euler theorem (integral form of the momentum conservation)

$$\underbrace{\partial_t(\overline{\tilde{\varrho}\tilde{v}})}_{\mathrm{E}}+\underbrace{\overline{\partial_x(\varrho\tilde{u}\tilde{v})}+\overline{\partial_y(\varrho\tilde{v}^2)}}_{\mathrm{C}}+\underbrace{\overline{\varrho v w(Z)}}_{\mathrm{B}}-\underbrace{\overline{\varrho_s v_s w_s}}_{\mathrm{G}} \qquad (1)$$

$$+\underbrace{\overline{\partial_y\tilde{p}}+\overline{\varrho\tilde{f}u}}_{\mathrm{H}}+\underbrace{p_s\overline{\frac{\partial h}{\partial y}}}_{\mathrm{F}}=0,$$

where for clarity $\overline{\partial_x(\varrho\tilde{u}\tilde{v})}$ represents the horizontal average of $\partial_x\left(\int_{h(x,y)}^{Z}(\varrho uv)\,\mathrm{d}z\right)$, etc. The different terms in (1) are expressed in Pa (momentum flux, or force per unit surface). They represent the time evolution (E), the horizontal momentum flux divergence (C), the vertical flux of momentum (B), the surface turbulent friction (G), the ageostrophic force (H), and the surface pressure drag (F). As explained in the introduction, some of these terms are accessible by measurements, for certain areas. For instance, since the y axis is parallel to the central transect, the surface pressure drag is available from the CNRM portable network measurements (see Sect. 2.2 and Fig. 17). The vertical flux of momentum above the central

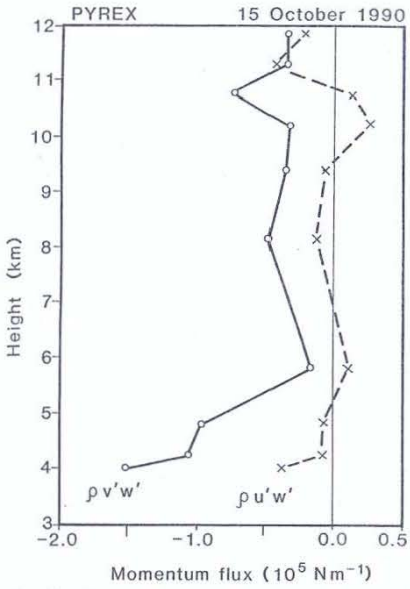

Fig. 19. Wave momentum fluxes computed from the Fokker and Falcon flights above the central transect

Table 4. The net force per unit length perpendicular to the track (F_x, F_y), the drag per unit area (D_x, D_y), and the total drag (M_x, M_y). The total drag is computed assuming a west-east extension of the Pyrénées of 300 km. The indices $x(y)$ correspond to the zonal (meridional) component

Altitude m	F_y 10^5 N m^{-1}	M_y 10^{10} N	D_y Pa	F_x 10^5 N m^{-1}	M_x 10^{10} N	D_x Pa
11 800	−0.35	−1.05	−0.19	−0.31	−0.92	−0.16
11 200	−0.37	−1.10	−0.20	−0.43	−1.28	−0.23
10 600	−0.72	−2.17	−0.39	0.11	0.33	0.06
10 000	−0.32	−0.94	−0.17	0.26	0.77	0.14
9 400	−0.34	−1.03	−0.18	−0.08	−0.23	−0.04
8 200	−0.48	−1.43	−0.25	−0.12	−0.36	−0.06
6 000	−0.15	−0.46	−0.09	0.08	0.24	0.04
5 000	−0.97	−2.91	−0.53	−0.08	−0.23	−0.04
4 400	−1.07	−3.21	−0.71	−0.09	−0.28	−0.06
4 000	−1.48	−4.43	−0.81	−0.38	−1.14	−0.21

transect can be computed from the horizontal and vertical velocities measured by the Fokker and Falcon airplanes, although this kind of computation usually involves a lot of uncertainties. To minimize these uncertainties, we removed the mean and trend, using a quadratic regression, and suppressed small-scale waves (smaller than 5 km) with a low-pass filter. The results are shown in Table 4 and Fig. 19. The surface pressure drag is about 6 Pa, whereas the wave momentum flux decreases from −0.8 Pa in the lower troposphere to −0.2 Pa between 6 and 10 km, and has a secondary maximum of −0.4 Pa at 11 km. Thus, the wave momentum flux is only a small fraction of the surface pressure drag, in agreement with the findings of Hoinka and Clark (1991) over the Alps.

The other terms of the budget must be deduced from model results. We have developed a diagnostic computation of these terms using the results of the Péridot model of Météo-France (Stein, 1989). For any desired box, consisting of a rectangular subdomain of the computation grid, the terms of Eq. 1 are computed for all heights Z above the highest topography present in this subdomain, and a residual is computed to assess the validity of this off-line computation. The residual is usually found to be very small. These computations have been performed by Beau (1992) on the simulation discussed above in Sect. 3.1, with various boxes shown in Fig. 20. The smaller box is called the validation box. It is designed to provide a computation as comparable as possible to the central transect measurements. Results for this box are shown in Fig. 21. Note that all values represent quantities integrated from the surface to the level given in ordinate, not local quantities. The surface terms (pressure and frictional drag) are therefore constant with height, and the vertical flux (B) has its usual meaning. These results can be compared with the observed values of Table 4 and Fig. 19. The model accurately reproduces the surface pressure drag of about 6 Pa, but it overestimates the wave momentum flux in the low levels by a factor of 2. It correctly reproduces the decrease in altitude of this flux, reaching very small values between 6 and 9 km, and increasing again above 9 km. It is very encouraging that the model vertical momentum flux is so similar to that observed. Also, it is interesting that the model predicts a variation of this flux with altitude, although there is no wave breaking in this case, and the dissipation of wave energy by the turbulence remains very small. This illustrates how much the 3D dynamics of these phenomena differ from the conventional 2D dynamics. In this case, the budget is closed by the ageostrophic pressure force and the horizontal momentum advection, and the situation is clearly not stationary in the higher levels. This means that the real problem is not to understand why the wave momentum flux differs from the surface pressure drag in observations, but to understand whether the model must still be improved to get quantitative agreement with observations of the vertical momentum flux (without changing the value of the pressure drag!), or if it should be accepted that the observed momentum flux in the lower levels is underestimated.

If we temporarily accept that the model is a good representation of reality, the budget can be computed at the scale of the entire range, using the large box of Fig. 20. The results, in Fig. 22, are very similar to those of the smaller box, but scaled down. This determination of the budget has been used by Beau (1992) for a preliminary study of the merits of several parameterizations of subgrid scale mountain waves in larger-scale models.

An independent determination of the momentum budget has been made by Benoit (1992), from data interpolated from the 11 soundings only. He made a 2D univariate analysis of pressure, density, altitude, and wind vectors, using the thin plate vector spline technique of Amodei and Benbourhim (1991), along sigma levels over the same horizontal domain as the numerical model. He then used the same diagnostic computation of the different budget terms. His result is shown in Fig. 23. For the lower levels, it is very comparable to the model-derived budget (Fig. 22). It is very encouraging to find that the shape of

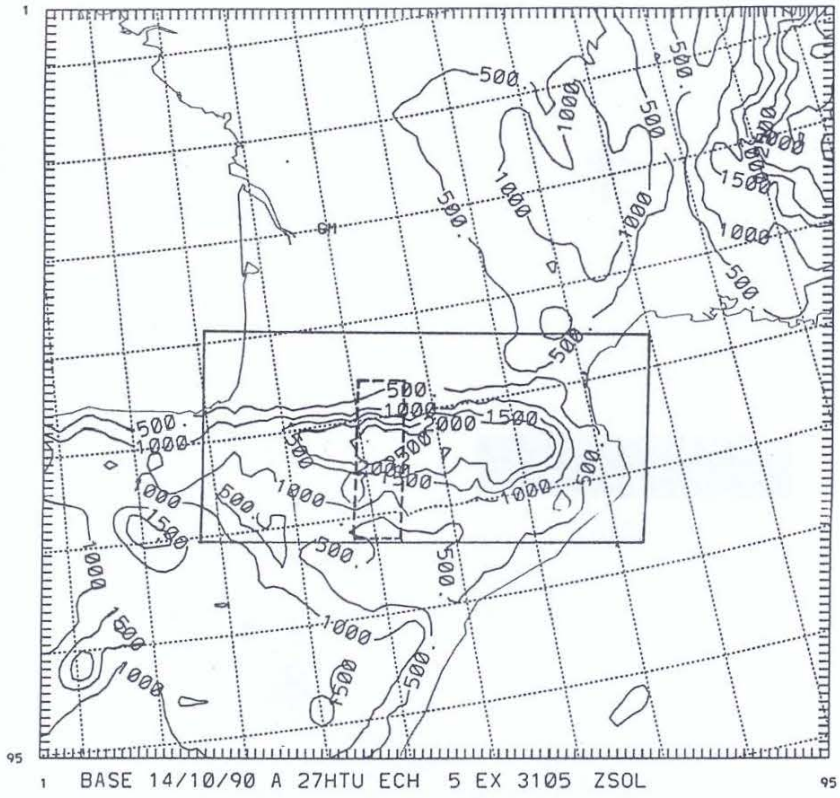

Fig. 20. Horizontal domains for the momentum budget computations with the outputs of the Péridot model. The *smaller box* is the validation box covering only the central transect. The *larger box* is well suited for an evaluation of the global effect of the mountain

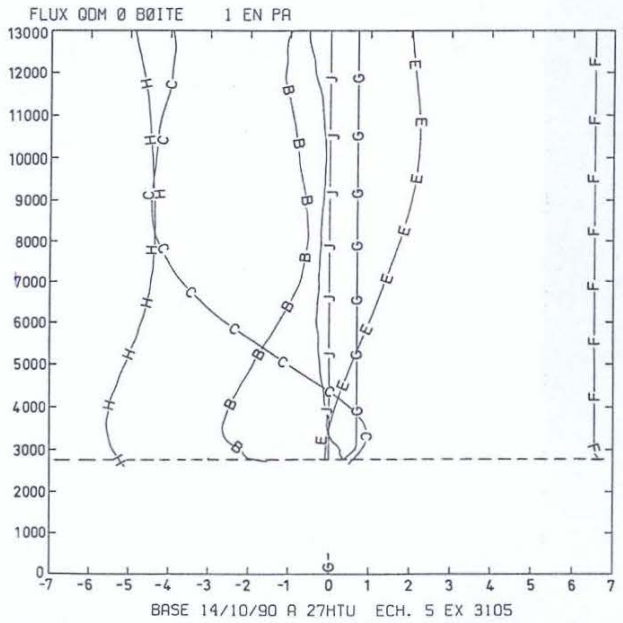

Fig. 21. Momentum budget computed in the validation box from the outputs of the model (see text). From Beau (1992)

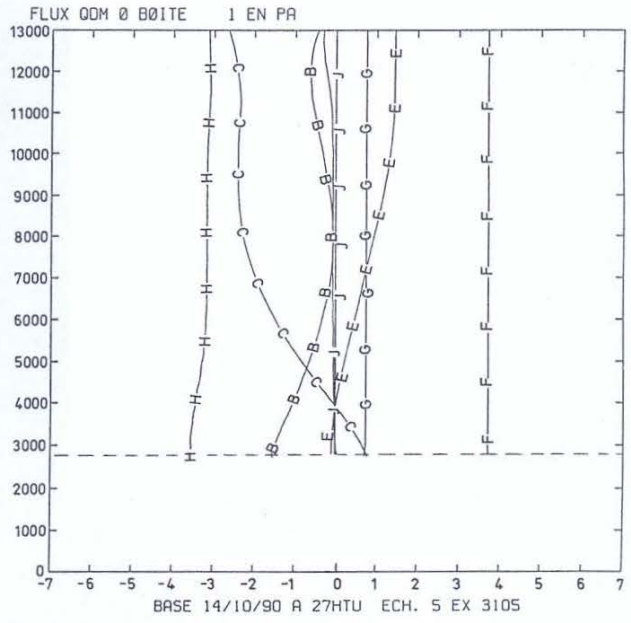

Fig. 22. Same as in Fig. 21, but on the larger box

the wave momentum flux is again very close to the aircraft determination of Fig. 19 (the values cannot be compared, since this is a much larger box). The surface pressure drag is nearly the same as in the model large box case, but the low level wave momentum flux is about half that of the model, which would tend to confirm that the model value is too large. The agreement is not so good in the upper levels, mainly because of the ageostrophic force and time variation terms. This results in a strong residual term, indicating that the budget is not closed in the upper

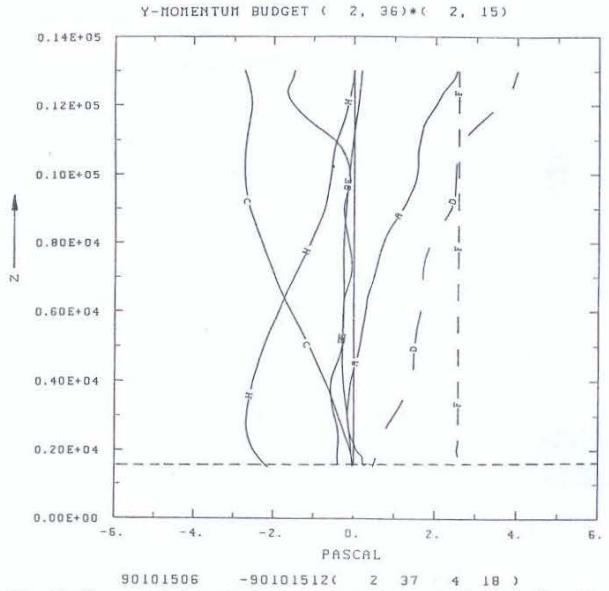

Fig. 23. Same as in Fig. 22, but obtained by interpolation of available soundings (from Benoit, 1992)

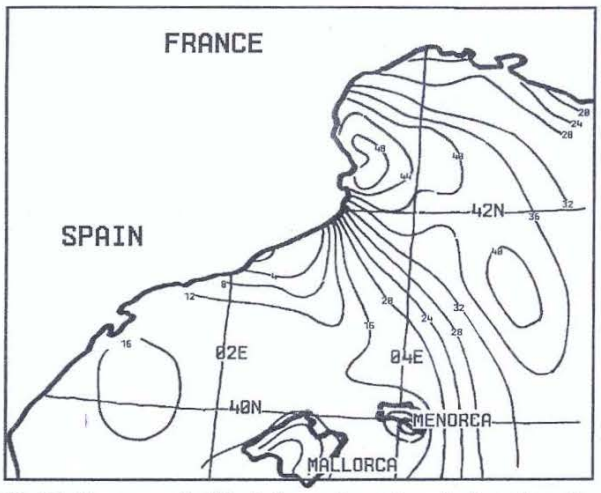

Fig. 24. Frequency (in %) of observations of northerly and northwesterly winds of more than 7 m s^{-1} (adapted from Marchionini and Gonzalez, 1991)

Table 5. Correlation between the drag and the strength of the Tramontana

IOP	Date	Average drag (Pa)	Maximum speed (m s^{-1})
1	5 Oct	4–5	20–22
6	4 Nov	2	15–20
6	5 Nov	0–1	8–12
8	12 Nov	2–3	10–15
9	14 Nov	4–5	20–22
9	15 Nov	5–6	22–27
9	16 Nov	6–7	25–27
10	29 Nov	2–3	10–17
10	30 Nov	5–6	20–22

atmosphere. Present work is directed at understanding this problem. Nevertheless, it is clear that this kind of model/data comparison will be a very efficient source of progress in the near future.

4 A closer look at Tramontana

The Tramontana wind is one of the major meteorological dangers of the western Mediterranean. The existing information on this phenomenon have been summarized by Jansa (1987). Figure 24, from the recent work of Marchionini and Gonzalez (1991), summarizes the climatology of the Tramontana through the frequency distribution of strong northerly and northwesterly winds. In the case of northerly synoptic flow, the positive pressure anomaly which forms on the north of the Pyrénées contributes to increase the pressure gradient on the abrupt eastern edge of the range. The resulting acceleration creates the Tramontana, which blows from north-west inland in France and turns north into the sea from the Gulf of Lion to the Balearic Sea. The PYREX data will be extremely useful to contrast previous ideas on this flow, and to validate the ability of numerical models to capture its intensity and extend.

4.1 Climatological aspects

A first result concerns the good correlation between the mean wind speed in the Tramontana and the drag observed on the central transect. This is shown in Table 5. The two quantities are nearly proportional, which confirms that the Tramontana flow is largely driven by the Pyrenean pressure anomaly. The maximum wind speed is usually found in the Gulf of Lion, close to the eastern edge of the range (Cape Creus), but this maximum is only 106% of the average speed observed along the tracks of the constant level balloons. The largest value observed during PYREX was around 26 m s^{-1} during the last two days of IOP 9. From the French coast to the maximum wind zone, the Lagrangian acceleration is then about 10^{-4} m s^{-2}. Accelerations about 10 times this value are needed inland, to produce the strong winds observed on the coast.

Another finding concerns the variation of the flow direction as a function of the synoptic situation. An inspection of the constant-level balloon tracks suggests the existence of two types of Tramontana. Indeed, the superposition of the low level (950 hPa) tracks of IOPs 1, 6, 9 (first two days) and 10 (day 2) gives a high coincidence (Fig. 25), revealing winds turning from NW to NNW. A second ensemble of tracks is found in IOPs 8, 9 (day 3), and 10 (day 1), indicating winds from due north over the sea. These differences are clearly related to the direction of the synoptic flow.

The Piper flights confirm these elements, and reveal details of the horizontal distribution of the flow. The most spectacular aspect of this structure is the sharp shear line starting from Cape Creus. Crossing this line from east to west, the wind decreases from more than 20 m s^{-1} to

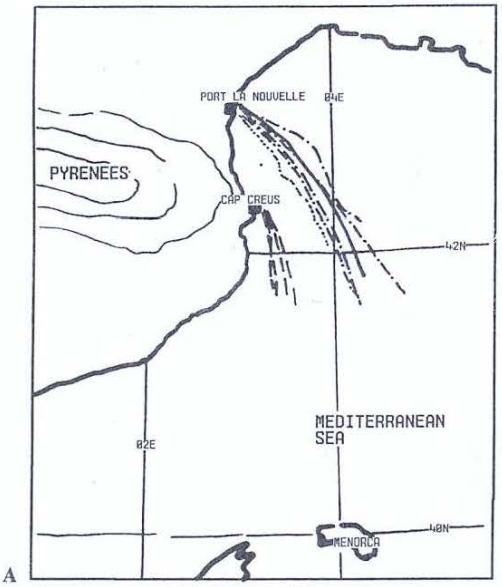

A

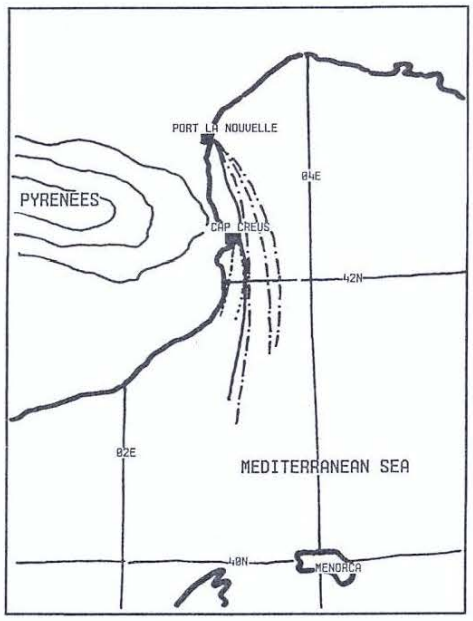

B

Fig. 25 A, B. Tracks of the constant level balloons flying between 895 hPa and 965 hPa. **A** type 1, **B** type 2. In **A**, the *solid line* corresponds to IOP1 flights, the *dashed line* to IOP6, the *dash-dotted line* to IOP9 (14th and 15th November), the *dotted line* to IOP10 (30th November). In **B** the *solid line* to IOP10 (29th November), the *dash-dotted line* to IOP9 (16th November), the *dotted line* to IOP8

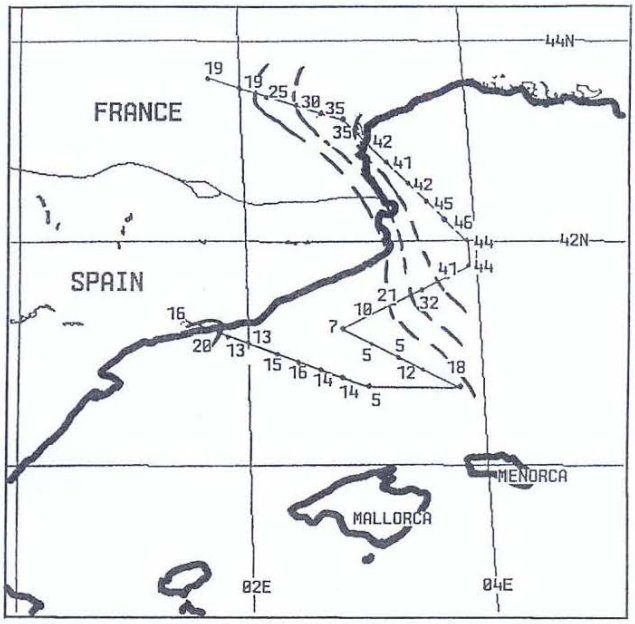

Fig. 26. An example of winds measured during the Piper Tramontana flight, showing the shear line developing from Cape Creus (the wind speed is given in knots along the aircraft track

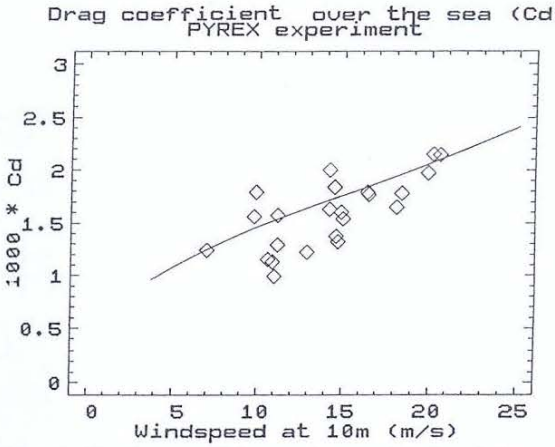

Fig. 27. The drag coefficient as function of the wind speed, measured during the Merlin Tramontana flights. The drag coefficient is defined as the ratio of the total momentum flux to the wind speed at 10 m, $C_D = u_*^2 / U_{10}^2$. For comparison, the *thin curve* shows the C_D value deduced from the Charnock formula, $z_0 = a u_*^2 / g$ (with $a = 0.0185$, the currently admitted value), combined with the logarithmic wind profile

5 m s^{-1} or so in a few km (Fig. 26). This shear line had been anticipated from previous work by Reiter (1971), and Jansa (1987). As the wind rotates so does the shear line from NNW in the type one cases, to NNE in the type two. This explains the statistical spreading of the shear in the frequency charts of the best available climatologies (Reiter, 1971; Marchionini and Gonzalez, 1991, see Fig. 24). In any particular case the shear line is well marked. Another difference between the two types is the elongation of the strongest wind zone towards the south. Thus, PYREX data confirms that from one case to the other, it is the whole wind system that rotates, not only the shear line. The most common situation belongs to what we have called type one.

Thanks to a large number of low level turbulence measurements, accurate determinations of the surface friction over the sea were possible during PYREX. Most of the data were acquired during the 3 Merlin Tramontana missions, which called for about 400 km flight at 40 m above sea level, an exhausting exercise for the pilots! The quality of these measurements has been checked by retrieving an equivalent drag coefficient from the turbulent momentum

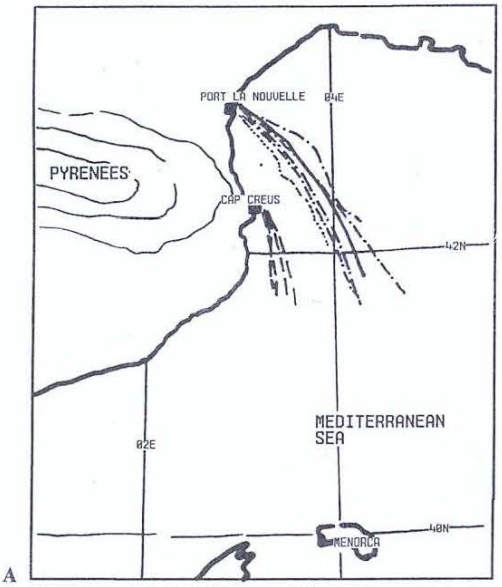

A

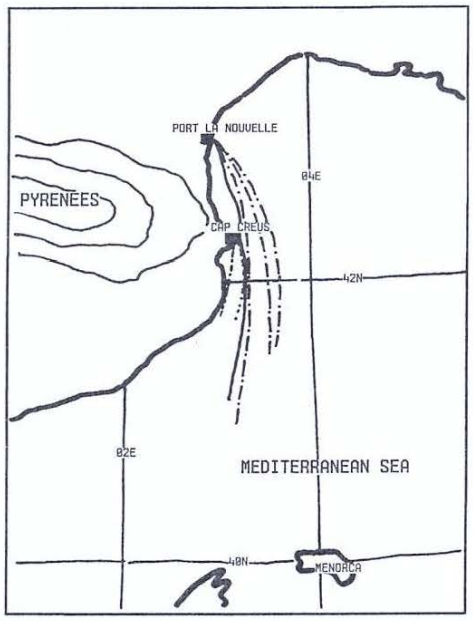

B

Fig. 25 A, B. Tracks of the constant level balloons flying between 895 hPa and 965 hPa. **A** type 1, **B** type 2. In **A**, the *solid line* corresponds to IOP1 flights, the *dashed line* to IOP6, the *dash-dotted line* to IOP9 (14th and 15th November), the *dotted line* to IOP10 (30th November). In **B** the *solid line* to IOP10 (29th November), the *dash-dotted line* to IOP9 (16th November), the *dotted line* to IOP8

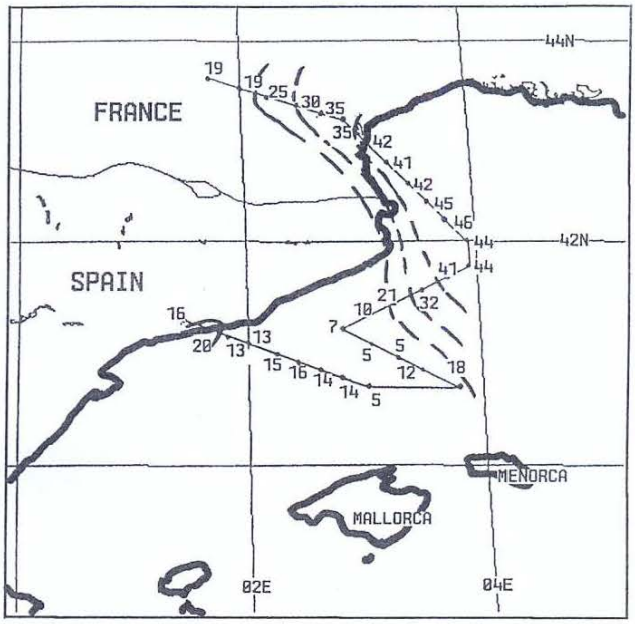

Fig. 26. An example of winds measured during the Piper Tramontana flight, showing the shear line developing from Cape Creus (the wind speed is given in knots along the aircraft track

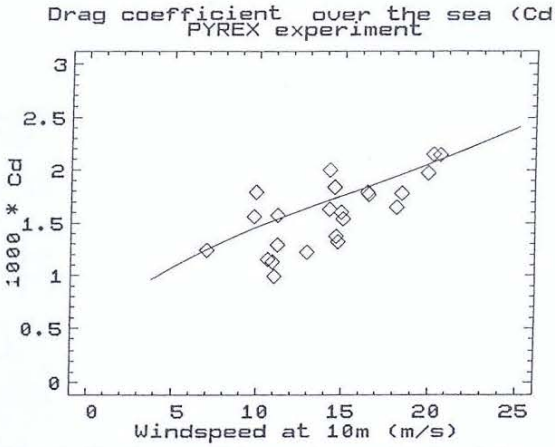

Fig. 27. The drag coefficient as function of the wind speed, measured during the Merlin Tramontana flights. The drag coefficient is defined as the ratio of the total momentum flux to the wind speed at 10 m, $C_D = u_*^2 / U_{10}^2$. For comparison, the *thin curve* shows the C_D value deduced from the Charnock formula, $z_0 = a u_*^2 / g$ (with $a = 0.0185$, the currently admitted value), combined with the logarithmic wind profile

5 m s^{-1} or so in a few km (Fig. 26). This shear line had been anticipated from previous work by Reiter (1971), and Jansa (1987). As the wind rotates so does the shear line from NNW in the type one cases, to NNE in the type two. This explains the statistical spreading of the shear in the frequency charts of the best available climatologies (Reiter, 1971; Marchionini and Gonzalez, 1991, see Fig. 24). In any particular case the shear line is well marked. Another difference between the two types is the elongation of the strongest wind zone towards the south. Thus, PYREX data confirms that from one case to the other, it is the whole wind system that rotates, not only the shear line. The most common situation belongs to what we have called type one.

Thanks to a large number of low level turbulence measurements, accurate determinations of the surface friction over the sea were possible during PYREX. Most of the data were acquired during the 3 Merlin Tramontana missions, which called for about 400 km flight at 40 m above sea level, an exhausting exercise for the pilots! The quality of these measurements has been checked by retrieving an equivalent drag coefficient from the turbulent momentum

fluxes and comparing it to the Charnock formula. These results are shown in Fig. 27, which demonstrates agreement with the expected values. These measurements will allow to take friction into account in a quantitative evaluation of the momentum budget of the accelerated flow, and to make extensive comparisons with the parameterizations used in numerical models.

4.2 The internal structure of the flow

Another interesting aspect of the Tramontana is linked to the bulk stability of the ABL. The northerly flow is generally colder than the sea surface temperature (differences of about 5 K were observed during PYREX). This creates a situation comparable to a cold air outbreak on the eastern sides of America or Asia, although the intensity of the heat flux is smaller. The ABL is unstable, and since the wind is strong, the situation is favourable to the development of coherent structures (such as helical vortices). These are materialized by cloud streets, which are visible on the NOAA10 image shown in Fig. 28. The structure of the marine ABL has been documented by aircraft, balloons and lidar during PYREX. An example of these measurements is given in Fig. 29, where the lidar range corrected cross-section is compared with in situ measurements taken by the Merlin and Fokker at different altitudes along the same track. The velocity component perpendicular to the mean flow at 37 m above sea level, the vertical velocity at 470 m, and the moisture at 940 m are shown: they are good indicators of the structures. Thanks to the good in-flight coordination, all these measurements were taken within a time span of less than an hour. The track extends from east to west, perpendicular to the mean flow. The figure shows two regions, east and west of 3.50 E. In the first part, the signal measured by the lidar is quite intense, with clouds forming at the top of the ABL represented as white regions. These clouds mark the presence of structures of about 3 km to 5 km in size. The in situ measurements also show periodic modulations of all parameters. At 940 m the flight leg to the east of 3.50 E lies clearly in the entrainment zone at the top of the ABL, as evidenced by the large humidity fluctuations, in good agreement with the cloud structure detected from the lidar. The coherent structures are also visible in the vertical velocity at 470 m, and in the transverse wind fluctuations near the surface. In the second part of the picture, west of 3.50 E, the intensity of the mean wind was rapidly decreasing due to the proximity of the mountain (this is the shear line discussed above). As a consequene, the surface heat and momentum fluxes were smaller, resulting in a decrease in the height of the ABL, which is visible in the first contour of the lidar cross section. There were no clouds in this part, and the 940 m flight leg was above the ABL top. However, less intense structures were still present, as shown by the contour oscillations in the lidar picture, and by the in situ measurements in the lower levels. A more detailed signal analysis will be necessary to ascertain these findings and obtain a comprehensive description of the coherent structures.

Fig. 28. Satellite picture from NOAA10, 4 November 1990, 0710 GMT (visible channel)

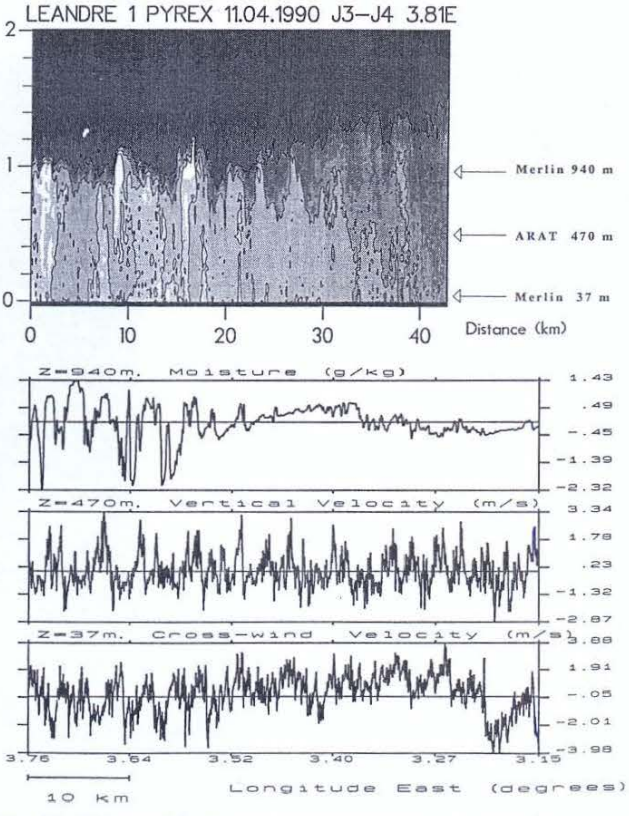

Fig. 29. Lidar and in situ measurements along a flight track crossing the wind from east to west on 4 November (IOP6). On the upper part is represented the lidar range corrected signal, obtained from the Fokker flying at 3200 m altitude. On the lower part are shown three detrended turbulent series obtained by the Fokker and the Merlin

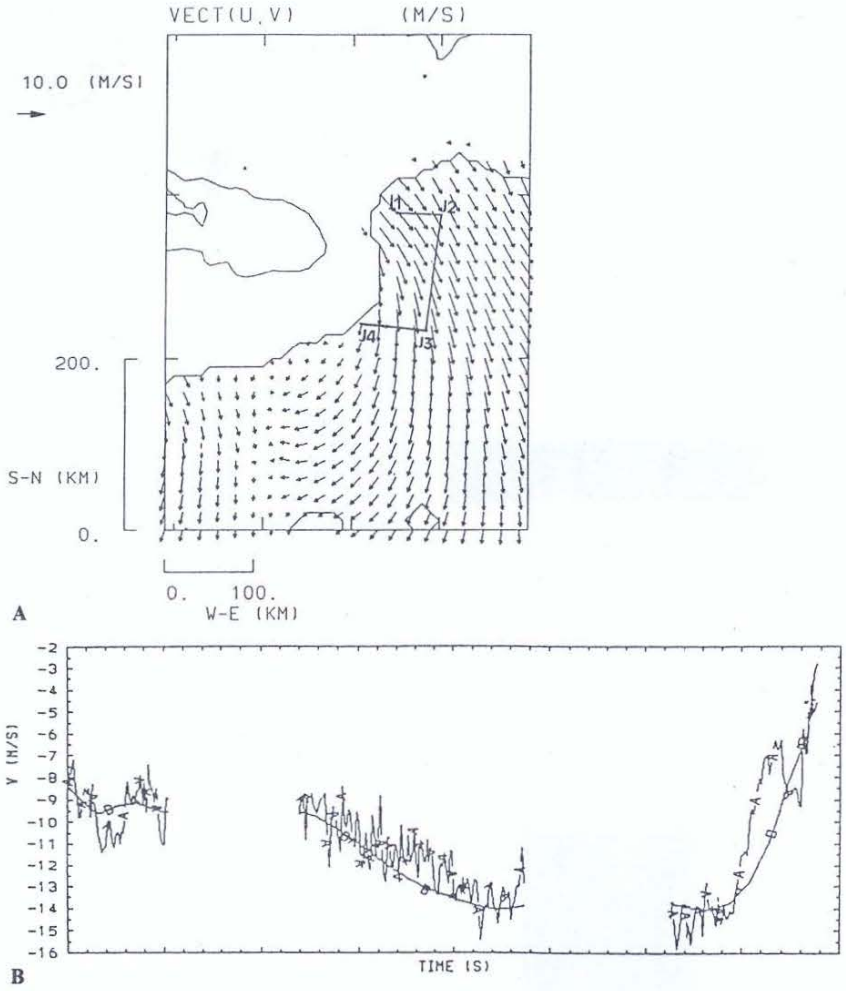

Fig. 30. **A** Surface wind simulated by the SALSA model of LA on 4 November 1990, 1200 GMT, **B** comparison of the observed (**A**) and simulated (**B**) northerly component of the wind on 4 November 1990 along the track J1-J2-J3-J4 shown in **A**

The case has been simulated by the SALSA meso-scale model of LA. An example of the wind predicted by this model near the surface of the sea is shown in Fig. 30. It reveals the formation of a lee-side eddy, reminiscent of the phenomena observed and simulated in the lee of smaller mountains (e.g. the Hawaii Island). The dynamics of this phenomenon is presently under study. The track of the Merlin Tramontana flight is also shown in Fig. 30, and detailed comparisons between the simulated and observed wind along this track are shown in Fig. 30 B. The intensity of the north-south component of the wind is well represented, and at the end of the flight leg, the simulated deceleration and rotation of the wind in the lee-side eddy are supported by the observation. The main discrepancy is located in the northern part of the flight, where the west-east component of the wind is clearly underestimated by the model. This may indicate an insufficient blocking by the Pyrénées, and will be studied in future work.

5 Conclusions

We have tried to illustrate both the diversity and the quality of measurements made during PYREX, and the general strategy for their scientific exploitation. The phenomenology documented by PYREX data is not new, but the complementarity of the observational means and the systematic use of numerical models open the way to an accurate evaluation of higher order quantities, like the terms of the momentum budget. Several problems remain to be solved concerning the measurements, whereas intercomparisons between data sources allow more precise assessment of their value. There is a place for much more detailed study of each data set, without the time and space resolution constraints imposed by our comparison with mesoscale models. Only such focused investigations can help to build the confidence in the various data sets, and to assess the value of our preliminary conclusions concerning the momentum budget. Several of these studies are already in progress (e.g. Attié *et al.*, 1992; Tannhauser and Attié, 1992; Flamant *et al.*, 1992). Others will be made possible by the decision of the project group to publicize the data base at the beginning of 1993. Requests for data are welcome, and we hope that this will foster cooperation with scientists involved in the study of orographic processes.

Acknowledgements. The PYREX experiment was made possible by the participation of a large number of institutes and funding agen-

cies. The participating institutes are CNRM, CRPE, LA, LAMP, LMD, LSEET, SA, EDF, France; INM, UV, UIB, Spain; and DLR, Germany (see list of acronyms). Funding was provided by Météo-France, INM, INSU (ARAT, PAMOS and PAMOY programs), CNES, EDF, DLR, and Région Midi-Pyrénées. Much technical help was provided by CEV, ENM, and the French and Spanish Airforce and Air Control authorities. We would like to express our gratitude to J. C. André, D. Cadet, D. Guédalia, and A. Ascaso Liria, for their help in the planning of this program. We also would like to express our deep appreciation to the many colleagues who have participated in the success of the experiment through enormous personal commitment.

References

Amodei L., and M. N. Benbourhim, A vector spline approximation, *J. Approximation Theory* **67,** 51–79, 1991.

Attié, J. L., B. Benech, A. Druilhet, and P. Durand, *Comptes-rendus scientifiques des expériences aéroportées réalisées avec l'ARAT et le Merlin IV pendant PYREX.* Laboratoire d'Aérologie, Toulouse, 1991.

Attié, J. L., A. Druilhet, B. Bénech, P. Durand, and F. Saïd, Evaluation expérimentale des transferts verticaux d'énergie dans un flux d'air normal à une chaine de montagne, in *22nd International Conference on Alpine Meteorolgy,* Météo-France, Toulouse, 18–22, 1992.

Beau, I., *Evaluation des paramétrisations de l'effet orographique sous maille dans les modéles de circulation généŕale à l'aide de Péridot 10 km,* Ecole Nationale de la Météorologie, Toulouse, 1992.

Benech, B., A. Druilhet, R. Cordesse, B. Dartiguelongue, J. Fournet-Fayard, J. C. Mesnager, P. Durand, and A. Malaterre, Un dispositif expérimental utilisant des ballons plafonnants pour l'étude de la couche limite atmosphérique, *Adv. Space. Res.,* **7,** 77–83, 1987.

Benech, B., J. L. Attié, A. Blanchard, P. Bougeault, P. Cazaudarré, A. Druilhet, P. Durand, E. Koffi, P. Prudhomme, and D. S. Tannhauser, Observation of lee waves above the Pyrénées (French Spanish PYREX experiment), *Technical Soaring,* 1993, in press.

Benoit, R., Mass and momentum budgets from high-resolution upper-air soundings over the Pyrénées, in *22nd International Conference on Alpine Meteorology,* Météo-France, Toulouse, 8–13, 1992.

Boer, G. J., N. A. McFarlane, and R. Laprise, The climatology of the Canadian climate center general circulation model as obtained from a five-year simulation. *Atmos. Ocean,* **22,** 430–473, 1984.

Bougeault, P., and R. Benoit, *La Base de Données PYREX,* CNRM/GMME, Toulouse, 1992.

Bougeault, P., A. Jansa Clar, B. Benech, B. Carissimo, J. Pelon, and E. Richard, Momentum budget over the Pyrénées: The PYREX experiment, *Bull. Am. Meteorol. Soc.,* **71,** 806–818, 1990.

Bougeault, P., and P. Lacarrère, Parameterization of orography-induced turbulence in a meso-beta-scale model, *Mon. Weather Rev.,* **117,** 1872–1890, 1989.

Bougeault, P., and C. Mercusot, *Atlas des analyses PERIDOT de l'expérience PYREX,* CNRM/GMME, Toulouse, 1992.

Buty, D., J. Y. Caneill, and B. Carissimo, Simulation numérique de la couche limite atmosphérique: Le code MERCURE, *J. Theor. Appl. Mech.,* **7,** 35–62, 1988.

Carissimo, B., J. M. Michelin, J. Jové, and D. Demengel, *Campagne PYREX: Atlas des données des stations du réseau EDF.* Techn. Rep., EDF HE 33/91.13, Electricité de France, Chatou, 1991.

Carissimo, B., R. T. Pierrehumbert, and H. L. Pham, An estimate of mountain drag during ALPEX for comparison with numerical models, *J. Atmos. Sci.,* **45,** 1949–1960, 1988.

Champeaux, J. L., and P. Peris, *Expérience PYREX: Atlas des données sol de Météo-France,* CNRM/GMME, Toulouse, 1991.

Clark, T. L., and M. J. Miller, Pressure drag and momentum fluxes due to the Alps. II: Representation in large-scale atmospheric models, *Q. J. R. Meteorol. Soc.,* **117,** 527–552, 1991.

Crochet, M., French program of a VHF transportable ST radar, *Handbook for MAP,* **9,** 400, 1983.

Davies, H. C., Observational studies and interpretation of the mountain pressure drag during ALPEX, in *Observation, theory and modelling of orographic effects,* ECMWF, Reading, 113–136, Reading, 1987.

Davies, H. C., and P. D. Phillips, Mountain drag along the Gotthard section during ALPEX, *J. Atmos. Sci.,* **42,** 2093–2109, 1985.

Durran, D. R., Two-layer solutions to Long's equation for vertically propagating mountain waves: How good is linear theory?, *Q. J. R. Meteor. Soc.,* **118,** 415–434, 1992.

Durran, D. R., and J. B. Klemp, The effects of moisture on trapped mountain lee waves. *J. Atmos. Sci.,* 39: 2490–2506, 1982.

Durran, D. R., and J. B. Klemp, Another look at downslope windstorms, Part II: Non linear amplification beneath wave-overturning layers, *J. Atmos. Sci.,* **44,** 3402–3412, 1987.

Elkhalfi, A., *Comparison hydrostatique non-hydrostatique avec le code MERCURE pour les écoulements sur relief complexe.* Thèse de Doctorat de l'Ecole Centrale de Lyon, 1992.

Flamant, C., J. Pelon, P. Flamant, and P. Durand, Boundary layer structure over the ocean observed by LEANDRE 1 during a Tramontana event, Ed. M. P. McCormick, *16th ILRC,* NASA Conf. pub. 3158, page 381, 1992.

Hoinka, K. P., Observational studies of mountain generated momentum fluxes, in *Observation, theory and modelling of orographic effects,* ECMWF, Reading, 1987.

Hoinka, K. P., and T. L. Clark, Pressure drag and momentum fluxes due to the Alps. I: comparison between numerical simulations and observations, *Q. J. R. Meteorol. Soc.,* **117,** 495–525, 1991.

Jansa, A., Distribution of the mistral: A satellite observation, *Meteorol. Atmos. Phys.,* **36,** 201–214, 1987.

Koffi, E., B. Benech, P. Bergue, B. Dartiguelongue, B. Dufour, D. Guedalia, G. Lachaud, N. Raynal, and C. Tarrieu. *Campagne PYREX: Traitement des données des ballons a volume constant relatives à l'étude du contournement,* Laboratoire d' Aérologie, Toulouse, 1991 a.

Koffi, E., B. Benech, J. Dessens, P. Malaterre, J. C. Mesager, G. Despaux, V. D. Pham, B. Campistron, and D. Tannhauser, *Campagne PYREX: Traitement des données des ballons à volume constant relatives à l'étude des ondes de sillage,* Laboratoire d'Aérologie, Toulouse, 1991 b.

Kotroni, V., and C. Mazaudier, Influence of orographic and canopy conditions on friction velocities observed during frontal events using Doppler Sodar observations, *J. Appl. Meteorol.,* 1992, in press.

Lilly, D. K., Wave momentum flux – A GARP problem, *Bull. Am. Meteorol. Soc.,* **53,** 17–23, 1972.

Lilly, D. K., J. M. Nicholls, R. M. Chervin, P. J. Kennedy, and J. B. Klemp, Aircraft measurements of wave momentum flux over the Colorado Rocky Mountains, *Q. J. R. Meteorol. Soc.,* **108,** 625–642, 1982.

Marchionini and P. Gonzalez, *Etude du système Mistral-Tramontane en Méditerranée,* Ecole Nationale de la Météorologie, Toulouse, 1991.

Palmer, T. N., G. J. Shutts, and R. Swinbank, Alleviation of a systematic westerly bias in general circulation and NWP models through and orographic gravity wave drag parameterization, *Q. J. R. Meteorol. Soc.,* **112,** 1001–1039, 1986.

Pelon, J., P. H. Flamant, and M. Meissonier, The French airborne backscatter lidar LEANDRE 1: conception and operation, Ed. V. E. Zuev, *15th ILRC,* NASA conf. pub. 3158, Cambridge, USA, page 36, 1990

Peltier, W. R., and T. L. Clark, The evolution and stability of finite-amplitude mountain waves. Part II: Surface wave drag and severe downslope windstorms, *J. Atmos. Sci.,* **36,** 1498–1529, 1979.

Petitdidier, M., V. Klaus, F. Baudin, C. Bourdier, M. Crochet, A. Desautez, C. Guérin, R. Ney, G. Penazzi, and P. Quinty, The 961/45 MHz bifrequency INSU/METEO stratospheric-tropospheric radar, *Meteorol. Rundsch.,* **42,** 142–151, 1990.

Puech, D., P. Bessemoulin, B. Dufour, and C. Tarrieu, *Catalogue des données du réseau sol 4M recueillies pendant l'expérience PYREX,* CNRM/GMEI, Toulouse, 1991.

Reiter, E., *Digest of selected weather problems of the Mediterranean,* Navy Weather Research Facility, Tech. Pap. 9/71, 1971.

Richner, M., The design and operation of a microbarograph array to measure pressure drag on the meso-scale, *J. Atmos. Ocean. Tech.,* 4:105–112, 1987.

Satomura, T., Compressible flow simulation on numerically generated grids, *J. Meteorol. Soc. Jap.,* **67,** 473–482, 1989.

Satomura, T., and P. Bougeault, Orographic wave drag during PYREX experiment, in Spring Meeting of the Meteorological Society of Japan, Tsukuba, p 282, 1992.

Shutts, G. J., Observations and numerical model simulation of a partially trapped leewave over the Welsh mountains, *Mon. Weather Rev.,* **120,** 2056–2066, 1992.

Smith, R. B. A measurement of mountain drag, *J. Atmos. Sci.,* **35,** 1644–1654, 1978.

Smith, R. B., Hydrostatic airflow over mountains, *Adv. Geophys.,* **31,** 1–41, 1989.

Smolarkiewicz, P. K., and R. Rotunno, Low Froude number flow past three-dimensional obstacles. Part I: Baroclinically generated lee vortices, *J. Atmos. Sci.,* **46,** 1154–1164, 1989.

Stein, J., *Etude numérique de deux cas d'écoulement hydrostatique sur les Pyrénées,* Ecole Nationale de la Météorologie, Toulouse, 1989.

Stein, J., *Contribution à l'étude des régimes hydrostatiques d'écoulements orographiques,* Thèse de Doctorat, Université Paul Sabatier, Toulouse, 1992.

Tannhauser and J. L. Attié, Optical and quantum mechanics analogs for trapped and leaky lee waves, in *22nd International Conference on Alpine Meteorology,* Météo-France, Toulouse, 1992.

Wallace, J. M., S. Tibaldi, and A. J. Simmons, Reduction of systematic errors in the ECMWF model through the introduction of an envelope orography, *Q. J. R. Meteorol. Soc.,* **109,** 683–718, 1983.

WMO, Scientific results of the Alpine experiment, GARP publication series, **27,** (2 volumes) available from WMO secretariat, Geneva, 1986.